

Site-specific dehydration of olivines from San Carlos and Kilauea Iki

Ferriss, Plank, Newcombe, Walker

Abstract

The rate at which hydrogen as H^+ moves into, through, and out of the olivine structure is of great practical interest for geologic applications such as quantifying the deep water cycle, assessing the fidelity of olivine-hosted melt inclusions, and estimating the decompression rate of volcanic eruptions. Here we conduct a series of experiments and observations on natural Fe-bearing olivine to better understand and quantify this H^+ movement, with a particular focus on the rate at which H^+ leaves olivine upon decompression, and including, for the first time, sequential dehydration experiments on single crystals of natural, Fe-bearing olivine. These efforts include four separate parts: (1) the partial hydration of polished blocks of xenolithic San Carlos olivine at 800°C and 1000°C, 1GPa, and oxygen fugacity (fO_2) at the Ni-NiO buffer (NNO); (2) sequential dehydration of a homogeneous block of San Carlos olivine at 800°C, 1atm, and fO_2 of NNO-2.6; (3) sequential dehydration of a polished block of an olivine phenocryst from Kilauea Iki at 800 and 1000°C, 1 atm, and fO_2 held at NNO-2.6 until the final step, which was conducted at NNO+1.9; and (4) the measurement by secondary ion mass spectrometry of hydrogen zonation profiles in an olivine phenocryst from Kilauea Iki coupled with Monte Carlo modeling and known decompression rates to determine bulk H diffusivities in a natural setting. Hydrogen zonation profiles were measured in all three crystallographic directions a , b , and c through the uncut blocks before and after each time step for all experiments by Fourier transform infrared spectroscopy using light polarized $\parallel a$ and modeled in 3 dimensions to determine both bulk and peak-specific H^+ diffusivities, producing over 50 sets of 3 diffusivities, one in each crystallographic direction.

The results show that diffusivities may vary both over time and for olivines with different defect structures, and so great caution should be taken before assuming H^+ diffusivities for a given olivine. However, we discovered 3 things: (1) the H^+ defect [Ti] that is associated with octahedral Ti can move into an olivine extremely rapidly, which suggests that octahedral Ti must be initially present and so may effect the speed at which H^+ may enter an olivine. (2) Changes in both bulk H^+ and peak-specific diffusivities during dehydration are related primarily to the buildup of Fe^{3+} and redistribution of the defects, particularly the rehydration of [Ti]. (3) The following Arrhenius laws appear to apply to bulk H^+ diffusion out of most olivines during decompression: $D_a = 10^{-5.4} \exp(130/RT)$; $D_b = 10^{-6.9} \exp(130/RT)$; and $D_c = 10^{-6.6} \exp(130/RT)$, where R is the gas constant; the units of the diffusivities (D) are in m^2/s ; and the activation energy is 130 kJ/mol.

Introduction

The diffusivity of hydrogen in olivine is a fundamental physical quantity critical for understanding a wide range of earth and planetary processes. Hydrogen can affect global-scale phenomenon such as melting relations and strength, and so in turn may control mantle rheology and the occurrence of plate tectonics (Keppler and Smyth 2006; Bell and Rossman 1992). Accurate knowledge of the diffusivity of hydrogen also has great potential to serve as a chronometer to determine magma ascent times from hydrogen diffusion profiles in olivine phenocrysts (Rosen 2016). Because of its close thermodynamic relationship to water and the bonds that H^+ forms with oxygen within the olivine structure, hydrogen incorporated in olivine and other nominally anhydrous minerals is sometimes referred to as “water” or “hydroxyl”. Here we will primarily refer to this species as H^+ .

H⁺ may be incorporated into the olivine lattice in a variety of ways that can be distinguished by differences in the absorbance of the O-H bonds as measured by Fourier transform infrared spectroscopy (FTIR) (Berry et al. 2005; Ingrin et al. 2013). Broadly, H⁺ defects fall into two categories: relatively high wavenumber peaks associated with silicon vacancies (sometimes called Group I bands) and relatively low wavenumber peaks associated with magnesium vacancies (sometimes called Group II bands). A doublet of peaks at 3525 and 3573 cm⁻¹ has been linked to the presence of 2 H⁺ ions, a Si⁴⁺ vacancy, and Ti⁴⁺ on a metal site (Berry et al. 2007). This mechanism, labeled [Ti], has been suggested to control mantle rheology (Faul et al. 2016). Multiple other high wavenumber peaks (3450-3620 cm⁻¹) represent 4 H⁺ ions charge-balanced by a Si⁴⁺ vacancy and are labeled [Si]. Some lower wavenumber peaks (3300-3400 cm⁻¹) appear when a Mg²⁺ vacancy is charge-balanced by a H⁺ and a trivalent cation on a Mg²⁺ site (Blanchard et al. 2017), and these are labeled [tri]. Low wavenumber peaks between 3200 and 3250 cm⁻¹ have been associated with 2 H⁺ charge-balancing a Mg²⁺ vacancy, and these are labeled [Mg]. The different mechanisms are important because the rate at which H⁺ moves through the lattice may vary for each defect (Padrón-Navarta, Hermann, and O'Neill 2014).

Previous work on the diffusivity of H⁺ in olivine has produced a 6-order-of-magnitude range of measurements, from 10^{-9.7} m²/s during the first hour of hydrating San Carlos olivine at 1000°C (Mackwell and Kohlstedt 1990) to 10^{-15.7} m²/s for [Si] loss from synthetic forsterite at the same temperature (Padrón-Navarta, Hermann, and O'Neill 2014). The calculated activation energies suggest even larger discrepancies at lower temperatures. This range has led to considerable disagreement about the correct diffusivity and approach to apply to a given application. The observation of differences in H⁺ loss profiles for different FTIR peaks (e.g., Tollan et al. 2015) is particularly important because if FTIR peaks must be resolved and analyzed individually, then H⁺ data from secondary ion mass spectrometry (SIMS), a common and powerful technique, becomes significantly more difficult to interpret because SIMS measures only the total, or bulk, H⁺.

Bulk H⁺ diffusion in natural olivine is often thought to occur by one of two mechanisms: a rapid “proton-polaron” mechanism (PP) that involves electron movement parallel to the crystallographic direction *a*, and a relatively slow “proton-vacancy” mechanism (PV) that relies on metal vacancy diffusion parallel to the crystallographic direction *c* (Kohlstedt and Mackwell 1998; Demouchy and Bolfan-Casanova 2016; Thoraval and Demouchy 2014; Demouchy and Mackwell 2006). Yet even within this PP versus PV framework, significant disagreement exists. For example, in studies of olivine phenocrysts, Le Voyer et al. (2014); Lloyd et al. (2013); and Hauri (2002) conclude that the most rapid H⁺ diffusion mechanism, PP, is likely operational, whereas Mironov et al. (2015); Portnyagin et al. (2008); Chen et al. (2011); and Gaetani et al. (2012) suggest that relatively slow PV diffusion is dominant. The major goal of this work is to better understand which diffusivity to use for applications that involve H⁺ diffusion in natural olivine.

Methods

We provide, for the first time, time-series data showing H⁺ loss from the same single crystal of Fe-bearing olivine. We do this for two olivines: a partially hydrated xenolithic olivine from San Carlos and a phenocryst from Kilauea Iki. These data are coupled with independent estimates of the H⁺ diffusivity based on H⁺ zonation patterns in a second Kilauea Iki phenocryst to produce a set of generic Arrhenius laws for H⁺ diffusion in natural olivine with forsterite numbers between 86 and 90.

Sample selection

Olivines from San Carlos, AZ and Kilauea Iki were chemically characterized and used for H⁺ diffusion experiments. The San Carlos olivine was provided by David Kohlstedt and is similar to that used in previous hydration experiments (Mackwell and Kohlstedt 1990; Kohlstedt and Mackwell 1998). Here we

extend that work by examining site-specific dehydration behavior. The Kilauea Iki olivines were collected from scoria from the 1959 Episode 1 eruption of Kilauea Iki and have been described in detail by David Ferguson (Ferguson et al. 2016), who provided the samples. The Kilauea Iki samples are of great interest because they provide the first direct experimental measurements of H^+ diffusion in all 3 crystallographic directions of inclusion-free olivine phenocrysts, and, because independent estimates of the decompression rate already exist (Ferguson et al. 2016). We can also estimate the hydrogen diffusivity in the olivine during its actual ascent.

Sample preparation

A large crack and inclusion-free piece of San Carlos olivine, SC1 (IGSN: IEFERSCO1), was oriented by Laue camera at Cornell University and then cut into a series of smaller pieces approximately 2-3 mm long on each side using a diamond saw. One of the resulting sub-pieces, SC1-1 (IGSN: IEFERJAI3), was polished with 0.25 μm diamond paste and used to estimate the initial H^+ concentration by FTIR. Additional pieces of SC1 were used to test the hydration procedure, and pieces SC1-7 (IGSN: IEFERJAI9) and SC1-2 (IGSN: IEFERJAI4) were partially hydrated and then polished with 0.25 μm diamond paste for FTIR. SC1-2 was then sequentially dehydrated with FTIR profiles measured after each dehydration step and afterwards analyzed by electron microprobe analysis (EMPA) and SIMS.

Two large, relatively clear pieces of the Kilauea Iki olivine were chosen and oriented based on crystal morphology. One of these samples, Kiki (IGSN: IEFERJAIC), was polished into a block shape of dimensions $2 \times 1 \times 1.3$ mm and characterized by EMPA, SIMS, and polarized FTIR. The orientation of this sample was confirmed by electron backscatter diffraction (EBSD) at the American Museum on Natural History. The sample was initially zoned in H^+ , and the low H^+ rims were polished off to create a homogeneous initial block for use in dehydration experiments.

This zonation was not polished off the second Kilauea Iki phenocryst, which was used to obtain an independent estimate of the bulk H^+ diffusivity in olivine as degassing took place during ascent. This sample was polished to its midpoint to expose the (010) plane and prepared for SIMS following recently developed sample preparation techniques for reducing instrumental background (Mosenfelder et al. 2011; Le Voyer et al. 2014; Newcombe et al. 2017). The phenocryst was cleaned in ultrasonic baths of toluene, acetone, and isopropanol; baked under vacuum at 110°C for ~72 hours; pressed into a 1-inch round aluminum mount containing indium metal; coated in Au; and allowed to degas in the sample exchange airlock for three days prior to analysis.

Sample thicknesses were measured with a digital micrometer accurate to within $\pm 5 \mu m$. Additional details for samples, including images and sample dimensions, are available online at geosamples.org.

Electron microprobe analysis

Major elements of SC1-2 and Kiki were analyzed by electron microprobe at AMNH along traverses parallel to those on which H^+ measurements were made to confirm homogeneity of the samples. The beam current was 20 nA, and the accelerating voltage was 15 kV.

Initial H^+ concentrations by FTIR and SIMS

The initial H^+ concentration in each olivine used in dehydration experiments was estimated using both polarized FTIR and SIMS. Polarized FTIR measurements were performed at AMNH using the Thermo Nicolet Nexus 670 infrared spectrometer and Thermo Nicolet Continuum 15 \times infrared microscope with a resolution of 4 cm^{-1} , spot sizes of $100 \times 100 \mu m$, an average of 200 scans, and a ZnSe polarizer. Initial H^+ concentrations were estimated from 3 orthogonal polarized measurements (Libowitzky and Rossman 1996; Shuai and Yang 2017) by applying the Bell and Withers calibrations (Bell et al. 2003; Withers et al. 2012). To account for the large error associated with baseline choice, 3

different baselines were drawn, and the resulting areas were averaged. Traverses along all three directions did not show significant zonation in bulk or peak-specific H^+ in the untreated samples.

Erik Hauri measured the C, H, F, P, and Cl concentrations by nanoSIMS along traverses parallel to c in SC1-2 and parallel to b in Kiki. SIMS measurements were made before Kiki was dehydrated but after the final dehydration heating step for SC1-2. The area under the O-H stretching peaks with the electric vector $E \parallel a$ is equal to that of both the untreated SC1-1 ($7 \pm 5 \text{ cm}^{-2}$) and of the partially hydrated and then dehydrated SC1-2 ($7 \pm 6 \text{ cm}^{-2}$). Therefore, the SIMS measurements of the hydrated and then dehydrated SC1-2 were taken as a reasonable estimate of the initial water concentration in SC1.

Hydration of San Carlos olivine

Two pieces of previously oriented San Carlos olivine SC1, SC1-2 and SC1-7, were partially hydrated in a $\frac{3}{4}$ " Boyd-type piston cylinder apparatus with a BaCO_3 pressure medium using a procedure broadly similar to that of Jollands et al. (2016). Here the samples were placed in copper capsules and surrounded by liquid distilled H_2O and a powdered mixture of Ni and NiO to control oxygen fugacity and San Carlos olivine and enstatite to control silica activity (Figure 1). Temperatures were controlled with a D-type thermocouple (W3%Re-W25%Re) with control precision of $\pm 2^\circ\text{C}$ and probable accuracy of $\pm 20^\circ\text{C}$. After rapid quenching followed by relatively slow decompression, the capsules were pierced with a drill to confirm water was still present and then dissolved overnight in a mixture of 1:1 H_2O to HNO_3 . The rectangular parallelepiped samples were then mounted in CrystalBond, polished with $0.25 \text{ }\mu\text{m}$ diamond paste on all sides, and cleaned in acetone.

SC1-2 was hydrated at a nominal temperature of 800°C and 10 kbar pressure, which corresponds to a water fugacity of 1.6 GPa (Withers 2013), for 17.5 hours. That time was chosen in order to reach, but not pass, what Kohlstedt and Mackwell (1998) call "metastable equilibrium", the point at which all of the initial Fe^{3+} is reduced as H^+ diffuses into the sample following the proton-polaron mechanism. If the model used by Kohlstedt and Mackwell (1998) is correct, the H^+ concentration in SC1-2 after the piston cylinder experiment should be homogeneous, and the concentration should be lower than the true solubility and presumably determined by the initial concentration of ferric iron. If the "metastable equilibrium" H^+ concentration is both large enough to easily measure and homogeneous, then SC1-2 is a suitable starting material for step-wise dehydration experiments.

SC1-7 was heated for 7 hours at 10 kbar and temperature readings of 1000°C , but the experiment ended when capsule began to melt, suggesting the true temperature in the capsule was closer to 1085°C , the melting point of copper or, more likely, the Cu was contaminated, perhaps with a small amount of oxygen, resulting in freezing point depression. This temperature range and pressure correspond to water fugacities of 1.9-2.0 GPa (Withers 2013). Within this temperature range, given the dimensions of the sample and the diffusivities reported by Kohlstedt and Mackwell (1998), the experiment time of 7 hours should allow the completion of proton-polaron diffusion and enter into the stage of diffusion dominated by the slower proton-vacancy mechanism without fully saturating the sample. This experiment allows a direct comparison with previous work (Kohlstedt and Mackwell 1998; Demouchy and Mackwell 2006).

Dehydration

Olivine samples SC1-2 (the same sample that was partially hydrated according to the procedure described above) and Kiki (untreated) were dehydrated in increments using the vertical furnace used in previous dehydration experiments (Ferriss 2015), and oxygen fugacity was controlled with a mixture of CO and CO_2 . The partially hydrated sample SC1-2 was heated at 800°C for 1, 3, 7, 13, 19, 43, and 68 hours at an oxygen fugacity $10^{-16.5}$ bars, equivalent to NNO-2.6, where NNO is the nickel-nickel oxide buffer. Kiki was heated at 800°C for 1 and 8 hours; then 3, 6, 7, and 8 hours at 1000°C . All heating steps for Kiki were conducted at oxygen fugacity of NNO-2.6 except for the final step at 1000°C , which was

conducted at relatively oxidizing conditions, NNO+2. A summary of all experimental run conditions is provided in Table 1.

Table 1. Experimental conditions for San Carlos olivine samples SC1-7 and SC1-2 and Kilauea Iki olivine Kiki

Sample name	Temperature (Celsius)	Pressure (GPa)	fO ₂ Buffer	log fO ₂ in bars	Heating time (hours)	Total dehydration time at constant temperature (hours)
SC1-7	1000	1	NNO	-10.3	7	-
SC1-2	800	1	NNO	-13.9	17.4	-
SC1-2	800	0.0001	NNO – 2.6	-16.5	1	1
SC1-2	800	0.0001	NNO – 2.6	-16.5	2	3
SC1-2	800	0.0001	NNO – 2.6	-16.5	4	7
SC1-2	800	0.0001	NNO – 2.6	-16.5	6	13
SC1-2	800	0.0001	NNO – 2.6	-16.5	6	19
SC1-2	800	0.0001	NNO – 2.6	-16.5	24	43
SC1-2	800	0.0001	NNO – 2.6	-16.5	25	68
Kiki	800	0.0001	NNO – 2.6	-16.5	1	1
Kiki	800	0.0001	NNO – 2.6	-16.5	7	8
Kiki	1000	0.0001	NNO – 2.6	-13.1	3	3
Kiki	1000	0.0001	NNO – 2.6	-13.1	3	6
Kiki	1000	0.0001	NNO – 2.6	-13.1	1	7
Kiki	1000	0.0001	NNO + 1.9	-8.4	1	8

FTIR

Before heat treatment and in between each heating step, samples were analyzed by polarized FTIR along 3 orthogonal traverses parallel to the three crystallographic directions in the uncut crystal. These analyses use the same conditions described above for estimating the initial water and were in all cases conducted with polarized radiation with the electric vector $E \parallel a$. Quadratic baselines were drawn based on the curve of the spectrum of the untreated and/or the dehydrated sample, with typical wavenumber ranges of 3200-3700 cm⁻¹. Each profile was normalized to the initial measurements to produce a ratio of the final to initial area A/A_0 and scaled up to a true concentration based on the initial concentrations, A_0 , determined above. These “whole-block” concentrations represent the average concentration through the entire path of the infrared beam and could be used to determine diffusivities in all three crystallographic directions following the fitting procedure described below.

To explore possible differences among various H⁺ defects, the same normalization and fitting procedures were applied to individual peaks using the peak heights relative to the quadratic baseline. Particular emphasis was placed on peaks at the following 4 wavenumbers: 3600, 3525, 3356, and 3236 cm⁻¹. The peak at 3600 cm⁻¹, designated [Si-Fe²⁺], is most likely 4H⁺ in a Si⁴⁺ vacancy with a nearby Fe²⁺

(Blanchard et al. 2017). The peak at 3525 cm^{-1} , designated [Ti-3525], is one of two prominent peaks produced by 2H^+ coupled with a Si^{4+} vacancy and a Ti^{4+} on a metal site. We focus on this peak both to minimize interference with nearby [Si] peaks and to more directly compare with the results of Padrón-Navarta, Hermann, and O'Neill (2014). The 3356 cm^{-1} peak, designated [tri- Fe^{3+} -3356], is the most prominent peak in a doublet associated with a Mg^{2+} vacancy charge-balanced by H^+ and Fe^{3+} substituting on a metal site (Blanchard et al. 2017), and the 3236 cm^{-1} peak, designated [Mg], is likely 2H^+ charge-balanced by a Mg^{2+} vacancy (Berry et al. 2005).

All of the raw FTIR spectra, baselines, and computer code used to produce all calculations and figures reported in this paper will be made available on GitHub.

SIMS

Hydrogen profiles along the a and c crystallographic axes in the naturally zoned Kilauea Iki phenocryst were characterized by SIMS using the Cameca 6f-SIMS at the Department of Terrestrial Magnetism, Washington DC. Analyses were performed using a primary beam current of $\sim 16\text{ nA}$. The primary beam was rastered across a $35\times 35\text{ }\mu\text{m}$ area during 300s of presputtering, and the area of the raster was reduced to $20\times 20\text{ }\mu\text{m}$ during analysis. Use of a circular field aperture with a $\sim 10\text{-}\mu\text{m}$ diameter ensured that only ions from the central $\sim 78\text{ }\mu\text{m}^2$ of the analytical crater were collected. Counts of ^{12}C , $^{16}\text{O}^1\text{H}$, ^{19}F , ^{30}Si , ^{31}P , ^{32}S , and ^{35}Cl were detected by an electron multiplier. A linear relationship between $^{16}\text{O}^1\text{H}/^{30}\text{Si}$ and H^+ concentration was defined by measurements of olivine and orthopyroxene standards (Koga et al. 2003). Background counts of $^{16}\text{O}^1\text{H}$ were assessed via frequent analysis of nominally dry Suprasil 3002 silica glass (purchased from Heraeus Quarzglas, Switzerland). Replicate analyses of Suprasil glass indicate that the detection limit of our water analyses was $1.5\text{ ppm H}_2\text{O}$ following the methodology of Long and Winefordner 1983. Analytical drift throughout the session was monitored via frequent analysis of Herasil 102 silica glass (purchased from Heraeus) containing $\sim 55\text{ ppm H}_2\text{O}$.

Diffusion modeling

H^+ diffusivities in each direction were obtained from the whole-block FTIR data after each time step using forward models modified to account for path integration effects. The 3-dimensional internal concentration, v , is calculated from the time t and diffusivities D in each direction for a rectangular parallelepiped with unit initial concentration and zero external concentration for the region $0 < x < L_a$, $0 < y < L_b$, $0 < z < L_c$ as follows (Carslaw and Jaeger 1959):

$$v = \left(\text{erf} \left(\frac{x}{2\sqrt{D_a t}} \right) + \text{erf} \left(\frac{L_a - x}{2\sqrt{D_a t}} \right) \right) \times \left(\text{erf} \left(\frac{y}{2\sqrt{D_b t}} \right) + \text{erf} \left(\frac{L_b - y}{2\sqrt{D_b t}} \right) \right) \times \left(\text{erf} \left(\frac{z}{2\sqrt{D_c t}} \right) + \text{erf} \left(\frac{L_c - z}{2\sqrt{D_c t}} \right) \right)$$

The internal concentrations are then averaged along the ray path of the FTIR observations to obtain path-integrated profiles. These “whole-block” profiles are then fit to the data measured in the uncut block. These models are described in more detail by E. Ferriss et al. (2015) and implemented using the free, open-source software package *pynams* (Ferriss 2015).

For the SIMS profiles of the zoned Kilauea Iki phenocryst, we estimated the diffusivity using a Monte Carlo model of diffusive H^+ loss from the olivine phenocryst in response to syneruptive degassing of its host magma. We assume an average decompression rate of $0.05 \pm 0.005\text{ MPa/s}$ from Ferguson et al. 2016 based on the diffusive loss of volatiles from olivine-hosted melt embayments (Ferguson et al. 2016) and that the volatile concentration of the host magma follows a closed-system degassing path (Witham et al. 2012). We use a 1-dimensional (1D) finite element model, which is appropriate if a central concentration plateau is observed, which would suggest that H^+ diffusion has not reached the center of the crystal (Thoraval and Demouchy 2014, Shea et al. 2015). The concentration of H^+ dissolved in olivine in equilibrium with the degassing magma, i.e., the boundary condition at the exterior edge of the crystal, is calculated at each time step with a partition coefficient K_d . The diffusivity of H^+ , the magma

decompression rate (dP/dt), and the partition coefficient are treated as free parameters in the model. Best-fit values of these parameters were determined via least-squares fitting to 20 synthetic water concentration profiles generated by assuming each H^+ concentration measurement is normally distributed with a mean corresponding to the measured value and a standard deviation of 0.35 ppm H_2O . The least-squares minimization was performed using the 'fminsearch' MATLAB function. Starting values of D , dP/dt , and K_d were drawn at random from the following uniform distributions spanning suitable ranges: $-9.5 < \log D \text{ (m}^2/\text{s)} < -10.5$; $0.045 < dP/dt \text{ (MPa/s)} < 0.055$; and $0.0012 < K_d < 0.0017$.

Results

Characterization of the starting material

Microprobe analysis did not reveal any significant zonation along the measured profiles and were generally consistent with previous work (Ruprecht and Plank 2013; Ferguson et al. 2016) with somewhat lower forsterite numbers: 87.7 ± 0.2 in SC1-2 and 86.2 ± 0.2 in Kiki (detailed traverse information and standard measurements are in the Supplemental Tables). The San Carlos olivine used in previous H^+ diffusion experiments had a reported approximate composition with forsterite number 91 (Mackwell and Kohlstedt 1990). This large difference in forsterite content suggests that the San Carlos olivine that we are using came from a different xenolith than the samples used in previous work. The initial water concentration was estimated from the polarized FTIR measurements and baselines shown in Figure 2 using both the Bell calibration and the Withers calibration and also by nanoSIMS (Table 2). These three estimates were averaged to produce initial H^+ concentration estimates of 15 ± 2 ppm H_2O in the Kilauea Iki olivine and 4 ± 1 ppm H_2O in the San Carlos olivine. These low concentrations are consistent with previous work on San Carlos olivine (Peslier and Luhr 2006; Kurosawa, Yurimoto, and Sueno 1997). The H^+ concentration in the Kilauea Iki sample, for which the low rims had been polished off to prepare the sample as a rectangular parallelepiped, was homogeneous by both SIMS and FTIR.

Several different O-H absorption peaks were observed in FTIR profiles of the initial materials. The prominent peaks at wavenumbers 3525 and 3573 cm^{-1} oriented primarily $\parallel a$ in both Kilauea Iki and San Carlos olivine correspond to the [Ti] incorporation mechanism, and the high-wavenumber peaks that primarily appear as shoulders on the [Ti] peaks correspond to [Si] (Berry et al. 2005). A very small peak at 3600 cm^{-1} present in both samples has been ascribed to [Si] with nearby Fe^{2+} (Blanchard et al. 2017). Because of the association with Fe^{2+} , we label this peak [Si- Fe^{2+}]. The Kilauea Iki olivine, but not the untreated San Carlos olivine, contains prominent [tri] peaks. These peaks at 3356 and 3329 cm^{-1} correspond exactly to the peak locations that Blanchard et al. (2017) associate with Fe^{3+} , and which we therefore designate [tri- Fe^{3+}]. No [Mg] peaks were present initially.

Table 2. H^+ concentration estimates for Kilauea Iki olivine and San Carlos olivine based on polarized FTIR areas (Figure 2) and SIMS measurements.

	Kilauea Iki olivine; Kiki	San Carlos olivine; sub-samples of SC1	
FTIR area E $\parallel a$ (cm^{-2})	52+/-10	7+/-5 55+/-17 24+/-8 7+/-6	untreated SC1-1 partially hydrated SC1-7 partially hydrated SC1-2 dehydrated SC1-2
FTIR area E $\parallel b$ (cm^{-2})	31+/-13	8+/-5	untreated SC1-1
FTIR area E $\parallel c$ (cm^{-2})	18+/-9	9+/-4	untreated SC1-1
FTIR area summed over 3 directions (cm^{-2})	101+/-19	24+/-8	untreated SC1-1
Water, Bell calibration (ppm H_2O)	19+/-4	4.5+/-1.5	untreated SC1-1

Water, Withers calibration (ppm H ₂ O)	12+/-2	3+/-1	untreated SC1-1
Water, SIMS (ppm H ₂ O)	14+/-1	5+/-1	dehydrated SC1-2
Average initial water (ppm H ₂ O)	15+/-2	4+/-1	SC1
Ratio of water in ppm H ₂ O to area in cm ⁻² with E <i>a</i>	0.3	0.6	SC1-1
Average water (ppm H ₂ O) after piston cylinder experiment	Not treated with pressure	32+/-23 14+/-10	partially hydrated SC1-7 partially hydrated SC1-2

Hydration

Changes in FTIR absorbance indicate that H⁺ was successfully incorporated into San Carlos olivine samples SC1-7 and SC1-2 (Figure 3A). To construct H⁺ profiles, quadratic baselines were drawn to match both the curve of the spectrum of the untreated sample and the middle baselines used to determine the initial water concentration in Figure 2. Typical baselines are illustrated in Figure 3B and C, and all spectra and baselines are shown in the Supplement. The area under each curve was determined and scaled to an estimated H⁺ concentration by multiplying by 0.6, following the ratio of concentration to area with E || *a* reported for San Carlos olivine in Table 2.

The partially hydrated sample SC1-2 was sufficiently homogeneous for both bulk H⁺ and individual peaks to serve as a reasonable starting material for subsequent dehydration experiments (Figure 4). If we ignore the uncertainties associated with baseline choice and use only the quadratic baseline shown in Figure 3C, the H⁺ concentration across hydrated SC1-2 is 15±1 ppm H₂O. Although there is a small increase in area around the [tri] peaks, the large majority of the H⁺ in the hydrated SC1-2 is present as [Ti] and [Si], and these profiles are also homogeneous.

In contrast, H⁺ zonation in SC1-7 is clearly observed, with water concentrations of 38±7 ppm H₂O using the quadratic baseline shown in Figure 3B. The variations in concentration are most apparent || *c* for bulk H and all major peaks (Figure 4), consistent with previously work showing *c* is the fast direction during proton-vacancy mechanism diffusion (Kohlstedt and Mackwell 1998; Demouchy and Mackwell 2006).

Quantifying the diffusivities in SC1-7 requires major assumptions about both the solubility and metastable equilibrium concentrations. Here we assume a metastable equilibrium concentration of 15±1 ppm H₂O, the observed concentration in SC1-2 after hydrating to saturate the PV mechanism. This value is much higher than the 0.4 ppm H₂O (7 H/10⁶Si) reported by Kohlstedt and Mackwell (1998), possibly because of differences in the forsterite content and/or the calibrations used to determine H⁺ concentrations from FTIR spectra in the two studies. The accepted values for PV (Demouchy and Mackwell 2006) fit our data reasonably well if we assume a final solubility of 150 ppm H₂O, which is possible, particularly given the still large uncertainties in the solubility of H⁺ in olivine (Tollan et al. 2017:20; Zhao, Ginsberg, and Kohlstedt 2004; Mosenfelder et al. 2006). Figure 4 shows the best fit to our whole-block SC1-7 data that assumes a final concentration equal to the maximum observed concentration of 58 ppm H₂O. This fit requires higher diffusivities than are generally associated with the PV mechanism, particularly || *b*. Diffusivities higher along *b* than *c* are unexpected but not entirely without precedent (e.g., Demouchy et al. 2016; Demouchy and Mackwell 2003) and not well constrained by three interior points.

Dehydration

SC1-2 and Kiki, two homogeneous blocks of olivine with similar initial starting H⁺ concentrations but very different histories, compositions, and distributions of H⁺, were sequentially dehydrated in a gas-mixing furnace (Figure 5). The choice of baseline is well known as a major source of error in FTIR

analyses, and associated errors in the resulting peak heights and areas may be as high as 30%, consistent across profiles. All profiles were normalized to a relatively homogeneous starting profile. While this error due to baseline selection is very large, it is a consistent offset for all estimates that is mostly eliminated by dividing by the initial values, which contain the same systemic error related to baseline choice.

Path-integrated 3-dimensional diffusion modeling was then performed on each profile to estimate the rate of H^+ movement after each heating step and associated errors (see Supplemental PDF). These efforts are described in more detail for each sample in the sections below. Much of the resulting diffusivities (see Supplemental Table) show H^+ loss rates that are *intermediate* between PP and PV mechanism diffusivities.

Dehydration of San Carlos olivine

We determined H^+ loss curves and diffusivities for bulk H^+ , $[Si-Fe^{2+}]$ at 3600 cm^{-1} , and $[Ti-3525]$ in San Carlos SC1-2. All spectra, baselines, profile data, and best-fit curves are provided in the Supplemental PDF. Selected profile data are shown in comparison with expected proton-polaron mechanism profiles in Figure 6, and all estimated diffusivities are shown as a function of heating time in Figure 7.

The $[Si-Fe^{2+}]$ peak clearly decreases more slowly than the rest of the peaks and was essentially immobile for the first 5 heating steps at 800°C . After 43 hours, when the large majority of the initial H^+ had left the crystal and the bulk of the remaining H^+ was present in the $[Si-Fe^{2+}]$ peak, clear H^+ -loss profiles could be observed for $[Si-Fe^{2+}]$, with apparent diffusivities that were relatively fast compared to the initial stages and with a fast direction $\parallel a$. These $[Si-Fe^{2+}]$ loss profiles also differ from the majority of profiles observed in this study in that they did not decrease to zero near the edges, but rather to about 40% of the initial concentration, which was the final concentration used when modeling the diffusivities. Over the course of the final heating steps, the rate of $[Si]$ movement increased noticeably, from $10^{-12.6}\text{ m}^2/\text{s}$ at 19 hours to $10^{-11.8}\text{ m}^2/\text{s}$ $\parallel a$ at 68 hours.

While the $[Si-Fe^{2+}]$ peak sped up, the $[Ti-3525]$ peak slowed down. To observe this decrease in H^+ loss rate in the profile data, compare the close correspondence of the $[Ti-3525]$ data with the expected PP curves at 7 hours with the large difference between the data and the PP curves at 19 hours (Figure 6D-F). The $[Si-Fe^{2+}]$ and $[Ti-3525]$ diffusivities eventually come close to converging, but the $[Ti-3525]$ peak diffusivity is always higher (Figure 7). Profiles for the other $[Ti]$ peak and additional $[Si]$ peaks in SC1-2 are not shown but behave similarly to $[Ti-3525]$.

The bulk H^+ curves, which consist of a combination of peaks, the $[Si]$ and $[Ti]$ peaks, show apparent diffusivities that are intermediate between the final $[Ti-3525]$ and $[Si-Fe^{2+}]$ mechanism diffusivities. The bulk H^+ curves are typically less symmetric than the profiles of either the $[Ti]$ or $[Si]$ peak, in part because of the occasional appearance of spectra with relatively large $[tri-Fe^{3+}]$ peaks and distorted baselines (see Supplemental PDF, e.g., $100\text{ }\mu\text{m}$ from the edge along a after 43 hours of heat treatment). This $[tri-Fe^{3+}]$ appeared intermittently near all edges of SC1-2 frequently enough that it is unlikely to be contamination but too infrequently to model with confidence. The final bulk H^+ concentration was modeled using 15% of the initial homogeneous partially hydrated concentration because the $[Si-Fe^{2+}]$ peak does not decrease to zero at the rim (as noted above), and therefore the bulk H^+ also cannot go to zero. During initial dehydration stages, when the $[Si-Fe^{2+}]$ peak at 3600 cm^{-1} was a relatively minor component, the bulk H^+ could be modeled well with PP, similar to $[Ti]$. By the end of the experiment, the bulk H^+ diffusivity had dropped from $10^{-10.9}$ to $10^{-11.6}\text{ m}^2/\text{s}$ $\parallel a$.

Experimental dehydration of Kilauea Iki olivine

Experimentation on the Kilauea Iki sample took place in two stages. First, the sample was treated exactly the same way as SC1-2 during dehydration: heated at 800°C in a gas-mixing furnace at NNO-2.6.

Second, the sample was sequentially heated at 1000°C, largely at NNO-2.6 (for 3, 6 and 7 total hrs) and then at NNO+1.9 for a final increment at 8 total hours. Heating the Kilauea Iki sample at 800°C for 8 hours did not produce any clear loss in bulk H or [Ti-3525] (Figure 8). Although bulk H⁺ and [Ti] did not change, heating the Kilauea Iki olivine at 800°C did result in significant re-organization, where the H⁺ from [tri-Fe³⁺] decreased by 50% and the H from [Si] doubled. The Kilauea Iki 800°C [tri] loss on reorganization rates were initially fast, around 10^{-11.0} m²/s || c at 1 hour before dropping to 10^{-12.5} m²/s at 8 hours. This drop in the [tri] movement rate suggests that the large majority of the internal H⁺ reorganization had been completed. The relative flatness of all of the profiles suggests that the movement was occurring everywhere throughout the crystal simultaneously, consistent with reorganization. The profiles from these 8 hours of heating at 800°C were used as the ‘initial’ profiles for data collected during a second stage of heating at a higher temperature.

The heating temperature was raised to 1000°C because the maximum bulk H⁺ diffusivities observed at 800°C were unlikely to produce clear H⁺ loss profiles within laboratory time scales. The oxygen fugacity was maintained along the same buffer curve, NNO-2.6, for 3 heating steps totaling 3, 6, and 7 hours, and in each of these steps, the rate of H⁺ loss could be estimated as 10^{-10.9} m²/s for bulk H⁺ and [Ti] and 10^{-10.7} m²/s for [Si-Fe²⁺] || to the fast direction *a*. These fits are shown in Figure 9 for the 6 hour data, and the rest are provided in the Supplement. The [Si-Fe²⁺] loss profiles in Kilauea Iki (Figure 9 J-L), unlike in San Carlos (Figure 6 G-I), appear to decrease to zero concentration at the rim, and to decrease at a rate faster than [Ti-3525]. The [tri] loss at 1000°C was slower than the other peaks and did not include an obvious fast direction.

A final heating step of 1 additional hour was performed for a total of 8 hours heating at 1000°C under more oxidizing conditions, NNO+1.9. The resulting loss of H⁺ for all mechanisms was consistent with the diffusivities determined under more reducing conditions, which suggests that the role of oxygen fugacity has little effect on the diffusivities, at least for this very late stage of dehydration and over such short timescales (1 hour).

Bulk H⁺ diffusivity in Kilauea Iki olivine during ascent

SIMS analysis of a natural Kilauea Iki olivine phenocryst along its crystallographic *a* axis indicates a central H⁺ concentration of ~11 ppm H₂O, decreasing to concentrations of ~6 ppm at the crystal edges (Figure 10). The H⁺ concentration gradients recorded in the outer ~200 μm of the crystal are suggestive of syneruptive water loss from the olivine in response to degassing of the host magma on ascent. Unlike the profile along *a*, the profile measured along *c* exhibits a constant H⁺ concentration. No decrease in H⁺ concentration was detected at the edge of the crystal along the *c* axis, suggesting that any signature of syneruptive degassing along the *c* direction may be confined to the region <~20 μm from the edge of the crystal, i.e., not resolvable at the spatial resolution of our analyses. These observations indicate that, under the conditions of generation of these H⁺ concentration gradients, the diffusivity of H⁺ parallel to *a* is greater than that parallel to *c*.

The plateau in H⁺ concentration supports our use of a 1D model, the results of which indicate a trade-off between *D* and *K_d*, with higher best-fit values of *K_d* resulting in higher best-fit values of *D*. No clear trade-off is observed between best-fit values of *D* and *dP/dt*. Our Monte-Carlo simulation suggests a H⁺ diffusivity || *a* of 10^{-10.17/+/- 0.08} m²/s at 1200°C.

Estimated bulk H diffusivity during dehydration of natural olivine

We use the H⁺ diffusivities determined at the end of each experiment, i.e., the data in San Carlos olivine SC1-2 after 68 hours of heating at 800°C and in the Kilauea Iki olivine after 8 hours of heating at 1000°C, combined with the diffusivity || *a* for the untreated Kilauea Iki olivine at 1200°C, to estimate rough Arrhenius laws for bulk H⁺ in natural Fe-bearing olivine in all three directions during dehydration (Figure 11). For convenience, we assume a constant activation energy of 130 kJ/mol and vary the pre-

exponential factor D_0 , which, as plotted in Figure 10, is $10^{-5.4} \text{ m}^2/\text{s}$ || a , $10^{-6.9} \text{ m}^2/\text{s}$ || b , and $10^{-6.6} \text{ m}^2/\text{s}$ || c . The errors on these estimates are difficult to estimate with only 2 to 3 data points, and additional data, particularly at high temperatures, would be very useful. The final diffusivity estimates for [Ti] and [Si] are similar to those for bulk H^+ and so are likely to follow similar Arrhenius laws.

Discussion

Comparison with previous work for bulk H^+

The Arrhenius laws for our final bulk H^+ diffusivities (Figure 11) are consistent with the large majority of previous observations of H^+ movement out of Fe-bearing olivines in nature. Thoraval and Demouchy 2014 extensively discuss 1- and 3-dimensional modeling of FTIR profiles of natural dehydrated olivine, with specific application to H^+ profiles in Pali-aike olivine measured by Demouchy et al. 2006 and including discussion of H^+ profiles measured by Peslier and Luhr 2006 and Denis et al. 2013. They conclude “The concentration profiles measured for Pali-aiki samples are characteristic of dehydration. However, they are neither consistent with PP process, which is too fast, nor with PV process, since a fast [001] axis is not observed.” Profiles reported in Peslier et al. 2008 and Peslier et al. 2015 could also be reasonably interpreted as having a fast direction || a rather than || c . These many observations of dehydration rates intermediate between PP and PV with a fast direction || a in natural samples are fully consistent with the results of the experiments presented here.

Our proposed Arrhenius laws are also consistent with the observation of H^+ distribution in and around melt inclusions by Le Voyer et al. 2014 and Lloyd et al. 2013. Le Voyer et al. 2014 used SIMS data to map the bulk H^+ around an olivine-hosted melt inclusion and found strongly anisotropic diffusion with a fast direction of a . They interpreted this observed anisotropy as dehydration occurring by PP, but the results presented here demonstrate that dehydration can occur with a fast direction || a and diffusivities slower than PP. Lloyd et al. 2013 document water loss from olivine-hosted melt inclusions as a function of the size of the pyroclast. Their implied diffusivity depends strongly on the choice of ascent rate in their model, requiring either short ascent times with PP or long ascent times with PV. Our results suggest that intermediate ascent times and diffusivities are also possible.

Hauri 2002, Portnyagin et al. 2008, Chen et al. 2011, Gaetani et al. 2012, and Mironov et al. 2015 use changes in the water concentration in the melt inclusions in unoriented olivines to estimate H^+ diffusivities in natural olivine. As discussed in some detail by Chen et al. 2011, diffusive anisotropy is very difficult to account for in these models, and the resulting estimates are likely to fall somewhere between the fast and slow direction diffusivities. Indeed, six of the seven diffusivity estimates produced from these melt inclusions studies fall between our estimated fast direction diffusivities || a and our slower direction diffusivities (Figure 11). Thus, the H^+ diffusivity estimates from Portnyagin et al. 2008, Chen et al. 2011, Gaetani et al. 2012, and Mironov et al. 2015 are all fully consistent with the results presented here. This agreement is remarkable given the wide variety of experimental conditions represented by these efforts, including both hydration and dehydration and oxygen fugacities ranging from QFM-7 (Chen et al. 2011) to QFM+3.3 (Portnyagin et al. 2008).

The only exception to the broad agreement of the above studies is a single, very fast estimate by Hauri 2002 for the dehydration of a melt-inclusion-bearing olivine from Loihi. This very rapid movement is difficult to understand with any certainty in the absence of either oriented profiles or FTIR spectra, but it does match well with PP mechanism diffusion observed during very early stages of dehydration in San Carlos olivine SC1-2. Thus, while most natural olivine is likely dehydrating at the intermediate rates shown in pink lines in Figure 11, H^+ diffusion may in at least some cases be faster, particularly during early stages of dehydration.

While more work remains to better understand and predict the variations in the rate of H loss from olivine, the frequent observation of rapid H⁺ loss and anisotropy from natural samples suggests that at least some of the H⁺ in a typical olivine dehydrating upon ascent is exiting via the proton-polaron mechanism, resulting in H⁺ diffusion with a fast direction || *a* and diffusivities faster than PV.

Comparison with previous work on peak-specific behavior

H⁺ loss or gain occurs from different FTIR peaks at different rates (Figures 6-9; Padron-Navarta et al. 2014; Hilchie et al. 2014; Tollan et al. 2015; Peslier et al. 2015; Jollands et al. 2016). Most of the peak-specific H⁺ diffusivities observed in this study are orders of magnitude higher than any of the diffusivities observed in synthetic forsterite (Figure 11). Peak-specific diffusivities may also change over time (Figure 7), most likely due to a redistribution of H⁺ among different defects and discussed further below. Thus, single values for peak-specific diffusivities measured in synthetic forsterite (Padron-Navarta et al. 2014; Jollands et al. 2016) are unlikely to apply to natural Fe-bearing olivines where PP is taking place and an increased number of defects and higher vacancy concentrations may speed up vacancy-facilitated diffusion.

Padron-Navarta et al. 2014, Hilchie et al. 2014, and Peslier et al. 2015 all observe faster movement of Mg-vacancy-related defects [Mg] and/or [tri] relative to Si-vacancy-related defects [Ti] and [Si] during dehydration. This observation is echoed in our PV hydration data for SC1-7 (Figure 4) but we were unable to test this result during dehydration of our SC1-2 sample because these peaks were either not present ([Mg]) or not systematically present ([tri]).

During the sequential dehydration of the Kilauea Iki olivine, we observe a clear fast direction || *a* in [Si] and [Ti] but not the [tri] peaks, which produce noisy, isotropic profiles with diffusivities that are, while still faster than would be expected from vacancy-controlled diffusivities in forsterite, roughly an order of magnitude slower || *a* than the [Ti] and [Si] peaks, in contrast to the observations of faster [tri] movement by other authors. The difference in anisotropy also suggests that the dominant mechanism by which in our SC1-2 sample leaves [tri] is different from that by which in our SC1-2 sample leaves the [Ti] and [Si]. Perhaps, for instance, in our SC1-2 sample leaves [Ti] and [Si] primarily by PP but leaves [tri] primarily during some redistribution process, for instance by moving from a Mg vacancy to a Si vacancy as discussed in more detail later in the discussion.

The SC1-2 partial hydration to metastable equilibrium resulted in minuscule amounts of [Mg] and [tri] (Figures 3 and 4) too small to give meaningful diffusivities during dehydration. The absence of these peaks from SC1-2 and large increase in [Ti] suggest that in San Carlos olivine, the vast majority of PP mechanism diffusion is affecting the [Ti] specifically. The reason for this close association is not entirely clear, but the [Ti] defect requires Ti⁴⁺ substituting onto an octahedral site (Berry et al. 2007 XANES paper). The fact that H⁺ is able to enter San Carlos olivine so quickly in the first hours of hydration by PP suggests that at least some octahedral Ti is initially present in San Carlos olivine. If all of the Ti were on the tetrahedral site initially, then some of that Ti would need to change its position in the crystal to create the [Ti] defect, a process that is unlikely to occur under the hour timescales at which PP is observed. Thus, any rapid influx of H⁺ by PP into an olivine may be limited not only by the initial quantity of Fe³⁺ (Kohlstedt and Mackwell 1998) but the initial amount of octahedral Ti.

The convergence of peak-specific rates in San Carlos olivine (Figure 7) suggests that in some applications peak-specific behavior may be safely ignored. An important exception may be the high-wavenumber [Si] peaks such as 3600 cm⁻¹ peak in the San Carlos olivine described here and the 3613 cm⁻¹ peak in forsterite described by Padron-Navarta et al. 2014. These peaks never came close to a rim concentration of zero in either of these experiments, and was particularly slow moving during early stages of dehydration. However, the 3600 cm⁻¹ peak first rises (at 800°C) and then drops (at 1000°C) significantly in the Kilauea Iki olivine, indicating that it can sometimes be very mobile. Additional work to understand peak-specific behavior is warranted, and any workers concerned with H⁺ diffusion in or out

of olivine or olivine-hosted melt inclusions should routinely obtain polarized FTIR profiles to help determine the importance of differences in individual peak behavior for a given olivine.

The transition from PP to PV during dehydration

We observe diffusivities significantly higher than those expected for vacancy-facilitated diffusion (Figure 11), which suggests that at least one mechanism is occurring that involves only the movement of H^+ and electrons, most famously as PP: $2H^+ + 2Fe^{2+} \rightarrow H_2 + 2Fe^{3+}$ (Kohlstedt and Mackwell 1998). The relationship between PP and PV is traditionally understood in terms of the abrupt transition, a sort of light switch that is set to either on or off, PP or PV. This clear transition has been observed for hydration (Figure 4; Kohlstedt & Mackwell 1998; Demouchy & Mackwell 2006), but our dehydration data are not not fully consistent with this model in terms of either edge concentrations or the rate of change in the diffusivities. Thoraval and Demouchy (2014) model profiles expected for such a transition (their Figure 6). Their models predict a fairly close equivalent to the metastable equilibrium concentration of hydration, in which very early stage dehydration profiles are not particularly well developed near the edge, reach a stage in which the profile is relatively flat with very steep drops on the edges, and then proceeds to drop by PV. The Kilauea Iki bulk H^+ profiles change very little during initial heating at 800°C, when Thoraval and Demouchy suggest that PP should be dominant, and then at 1000°C we observe reasonably well developed profiles from earlier on that appear to go to zero and are fairly consistent over time. The SC1-2 data had an initial hydrated concentration at “metastable equilibrium” rather than full solubility and might be expected to only proceed by PP until all of the H^+ had returned to its untreated level. Instead, the bulk H^+ diffusivity in SC1-2 appears to slow down over time. The behavior of H^+ and transition from PP to PV thus appears to be fundamentally different during dehydration than what might be expected from hydration experiments.

This difference may be attributed to the relative instability of Fe^{3+} in the olivine structure. PP during hydration, $H_2 + 2Fe^{3+} \rightarrow 2H^+ + 2Fe^{2+}$, may proceed rapidly to metastable equilibrium because the olivine structure can happily accommodate Fe^{2+} , whereas the reverse reaction requires a buildup of Fe^{3+} . The more Fe^{3+} that is already present, the less stable the overall structure, and the slower the reaction. This gradual slowing down may account for the decrease in H^+ diffusivity during dehydration of SC1-2. We can also understand the difference in behavior for SC1-2 (decreasing diffusivities with time from fast to relatively slow) and Kiki at 1000°C (constant relatively slow diffusivities) as a difference in initial Fe^{3+} concentrations, with SC1-2 starting with relatively little Fe^{3+} and thus experiencing more initial H^+ loss by PP. In contrast, PP may have been impeded in the significantly oxidized (Helz et al. 2017) Kilauea Iki olivine.

Because of this decrease in the bulk H^+ diffusivity, the transition from PP to PV during dehydration is less like a light switch and more like a dimmer switch, with a top setting of PP and bottom setting of PV. However, this analogy is not perfect because, as discussed in the next two sections, variations in H^+ diffusivities can also be affected by changes in the ferric/ferrous ratio and a competition between dehydration and rehydration associated with H^+ redistributing among defect sites.

Redox re-equilibration and common Arrhenius laws

An added complication is the potential for re-equilibration of the ferric/ferrous ratio with the outside (Gaetani et al. 2012) at rates likely to be set by vacancy diffusion (Uli Faul ref), which could reduce the Fe and allow PP to continue where it might otherwise have stopped on account of a local over-abundance of Fe^{3+} . Once the lattice of a given olivine's ability to accept Fe^{3+} has been saturation, PP in that olivine will then be limited by the rate at which Fe^{3+} can be re-introduced. This ferrous/ferric re-equilibration rate, if it is similar for different olivines, may at least partially explain the observation of a common set of Arrhenius laws for a variety of different olivines (Figure 11).

Redistribution of H⁺ among incorporation sites

In addition to PP and PV moving H out of the structure, a hydrous olivine moved into a lower pressure environment, e.g. 1 bar at Kilauea Iki (Ferguson et al. 2016), may improve its stability in part through a redistribution of the H⁺ among different sites. Such a redistribution can be seen in both the Kilauea Iki and San Carlos olivine.

Peak redistribution in Kilauea Iki

After 8 hours of heating at 800°C, Kilauea Iki olivine shows a clear decrease in the [tri] concentration and corresponding increase in [Si], while the [Ti] peaks and bulk H⁺ were essentially immobile (Figure 8), in striking contrast to the clear loss in [Ti] from San Carlos olivine SC1-2 under the same experimental conditions (Figure 6). After increasing the temperature to 1000°C, the [Ti] exhibited fast, anisotropic loss profiles from Iki (Figure 9). The reason for this jump in the [Ti] movement rate, from essentially immobile (all PV) to noticeable H⁺ loss by PP, is not entirely clear but may be related to the equilibration in the redox state of the crystal.

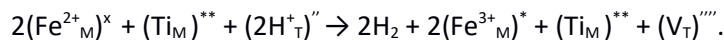
Although the experiments were run at relatively reducing conditions, at 800°C the kinetics of Fe oxidation state equilibration may have been too sluggish to produce enough Fe²⁺ in Kiki for PP to proceed efficiently. Alternatively, PP may have been occurring from [Ti] at 800°C, but that loss could have been masked by rapid redistribution of H⁺ from [Si] and/or [tri]. Both possibilities are difficult to test with the current data set. What is clear is that after an initial period of re-equilibration and redistribution and at the higher temperature more relevant to most geologic applications, [Ti] dehydration profiles show a clear fast direction || α and diffusivities intermediate between PP and PV.

Peak redistribution in San Carlos olivine

Immediately prior to dehydration, the H⁺ in San Carlos olivine SC1-2 was observed almost entirely as [Ti], which proved highly mobile with a fast direction || α . Most of the [Si] peaks behaved similarly to [Ti], with the exception of one small peak at 3600 cm⁻¹ (Figure 5). The increase in the rate of [Si] movement coupled with a decrease in the rate of [Ti] (Figure 7) suggests that at least some of the H⁺ leaving the [Si] is doing so by moving into other Si vacancies associated with [Ti] rather than leaving the crystal directly.

To describe this process in more detail, we use Kröger-Vink notation, which describes crystal defects as follows: V is a vacancy, a superscript * indicates a positive charge relative to an ideal crystal, ' indicates a negative charge relative to an ideal crystal, and ^x no charge difference from an ideal crystal. Subscripts indicate different sites: M for octahedral metal sites and T for tetrahedral. Atoms that are not involved in any reactions are ignored. For simplicity, all equations describing H⁺ incorporation here will assume H⁺ is occupying a related vacancy rather than an interstitial site. For example, the [Ti] site which involves a Ti⁴⁺ on a metal site, 2H⁺, and a Si vacancy, may be represented as (Ti⁴⁺_M)^{''}(2H⁺_T)^{''}.

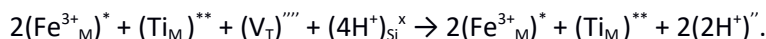
The initial hydrogen movement of [Ti] out of SC1-2 occurs at rates comparable to the classic PP mechanism (Figure 6 D-F), which increases the number of open tetrahedral site vacancies near octahedral Ti:



In contrast, the profiles for the high-wavenumber [Si] peak that was initially present in our sample (Figure 2A) did not change significantly during the initial stages of either hydration or dehydration, suggesting that H⁺ loss by PP from this site was impeded for reasons that are unclear.

The [Ti] mechanism is known from incorporation studies as a particularly favorable position for H⁺ (e.g., Berry et al. 2005). Because of the relative stability of [Ti], any H⁺ that are unable to leave readily by

PP from [Si] may prefer to move into recently-vacated Si vacancies that bring them closer to the octahedral Ti:



As H loss proceeds by PP from [Ti], the number of Si vacancies near octahedral Ti increases, and so the redistribution of H^+ from [Si] to [Ti] becomes easier and thus faster. This increase in Si vacancies is also likely to increase the rate of vacancy-facilitated diffusion of the H^+ in this [Si] peak out of the crystal.

Such a redistribution would explain the relative changes in rates that we observe between [Ti] and [Si] in Figure 7. The H^+ leaves quickly from [Ti] by PP throughout the duration of the experiment, but the peak appears to slow down as more and more H^+ moves into [Ti] from [Si]. Thus, the observed loss of the [Si] peak may not represent H^+ moving out of the sample at all, but rather may indicate rate at which the H^+ is redistributing between sites. This redistribution is slow enough to observe over a period of days because this experiment was conducted at the relatively low temperature of 800°C, but at magmatic temperatures and/or in samples with higher concentrations of H^+ in relatively unstable defects, the redistribution rates are likely to be higher.

Conclusions

We conducted a series of hydration and dehydration experiments to gain insight into the behavior of H^+ in natural olivine. The results indicate a great deal of complexity, even for just the two olivines used in our study. H^+ movement in other olivines may deviate considerably from our results given significantly different defect structures or under different pressure and temperature conditions, as was observed for instance in different H^+ behavior in the Kilauea Iki olivine at 800°C versus 1000°C. While there is still much that we do not understand, we can however draw three conclusions with some certainty.

First, the [Ti] mechanism, which is associated with octahedral Ti, can and does move very fast, at or near proton-polaron rates, during hydration. H^+ movement into this defect at these very fast rates requires that the Ti be present initially in an octahedral rather than tetrahedral site because the movement of H^+ is too rapid to allow for a reaction to occur in which Ti, or any other large ion, can move between sites. Thus, rapid hydration of olivine depends at least partially on the initial concentration of octahedral Ti.

Second, the rates at which both bulk H^+ and individual defects sites move can change over time and depending on the defect structure of the crystal. Thus, the use of constant peak-specific diffusivities measured in synthetic forsterite, e.g., as measured by Padron-Navarta et al. 2014 and applied in Tollan et al. 2015, is inappropriate for natural, defect-rich samples. Further, the changes in bulk H^+ diffusivities observed here for dehydration are different from the binary change of rates from proton-polaron to proton-vacancy suggested by Thoraval & Demouchy 2014 based on observations of hydration. Instead, the buildup of Fe^{3+} and redistribution of H^+ defects effectively slow down dehydration from proton-polaron rates.

Third, there appears to be a common set of Arrhenius laws that can be used to explain most experimental and natural data: $D_{[100]} = 10^{-5.4} \exp(130/RT)$; $D_{[010]} = 10^{-6.9} \exp(130/RT)$; and $D_{[001]} = 10^{-6.6} \exp(130/RT)$, where the units of the diffusivities are in m^2/s , and the activation energy, 130, is in kJ/mol. These Arrhenius laws are intermediate between the classic PP and PV models of diffusivity observed during hydration and are in good agreement with many observations of a fast direction || a in natural olivine. While variations in different H^+ incorporation mechanisms and other defects may produce potentially large variations in the bulk H^+ diffusivities for different olivines, the generic bulk H^+ Arrhenius laws determined here are expected to apply to most natural olivines and therefore should

provide reasonable starting estimates for applications such as the determination of decompression rates from H^+ zonation profiles.

Acknowledgments

This work was supported by National Science Foundation grant #1449699. Daniel Rasmussen performed the electron microprobe analyses.

Figures

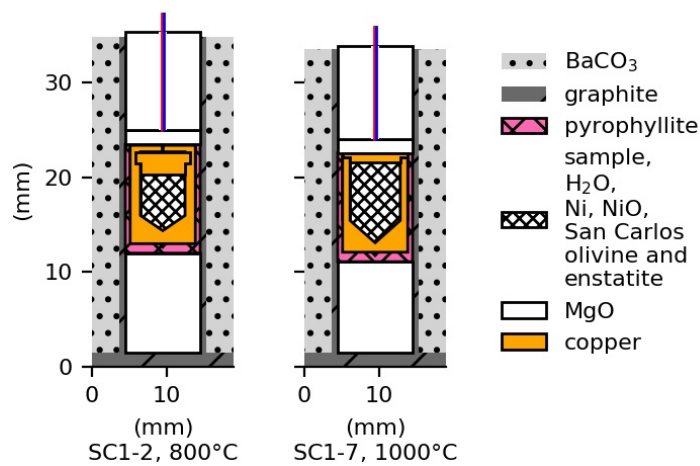


Figure 1. Schematic cross-sections illustrating the experimental design for hydrating San Carlos olivine samples SC1-2 and SC1-7 in a piston cylinder apparatus showing the $BaCO_3$ pressure medium, graphite furnace and pyrophyllite sleeve surrounding an unwelded copper capsule containing the sample, liquid water, and a powdered mixture of nickel, nickel oxide, San Carlos olivine, and San Carlos enstatite. The sleeve and capsule are supported by MgO, and D-type W-Re thermocouples (colored lines) extend through cylindrical holes in the MgO. Minor differences in the capsule shapes are a result of differences in Cu machining techniques.

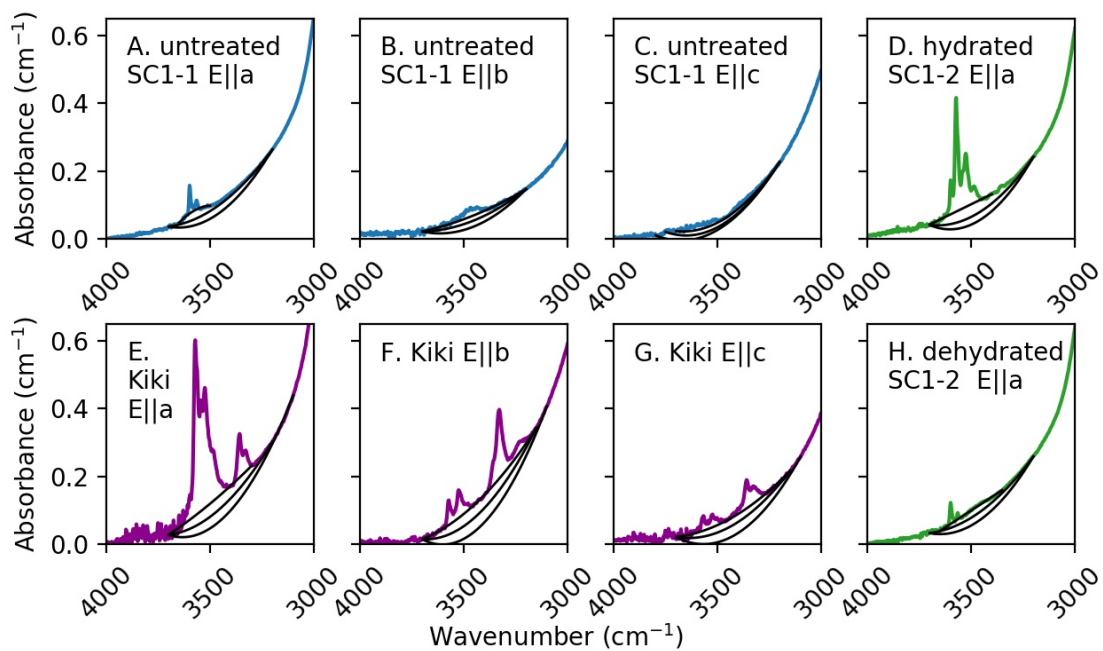


Figure 2. Polarized FTIR spectra and baselines (black) used to estimate the H^+ concentrations of Kilauea Iki olivine (Kiki) and San Carlos olivine (SC1-1 and SC1-2) reported in Table 2. E is the electric vector of the infrared beam, and a, b, and c are crystallographic directions.

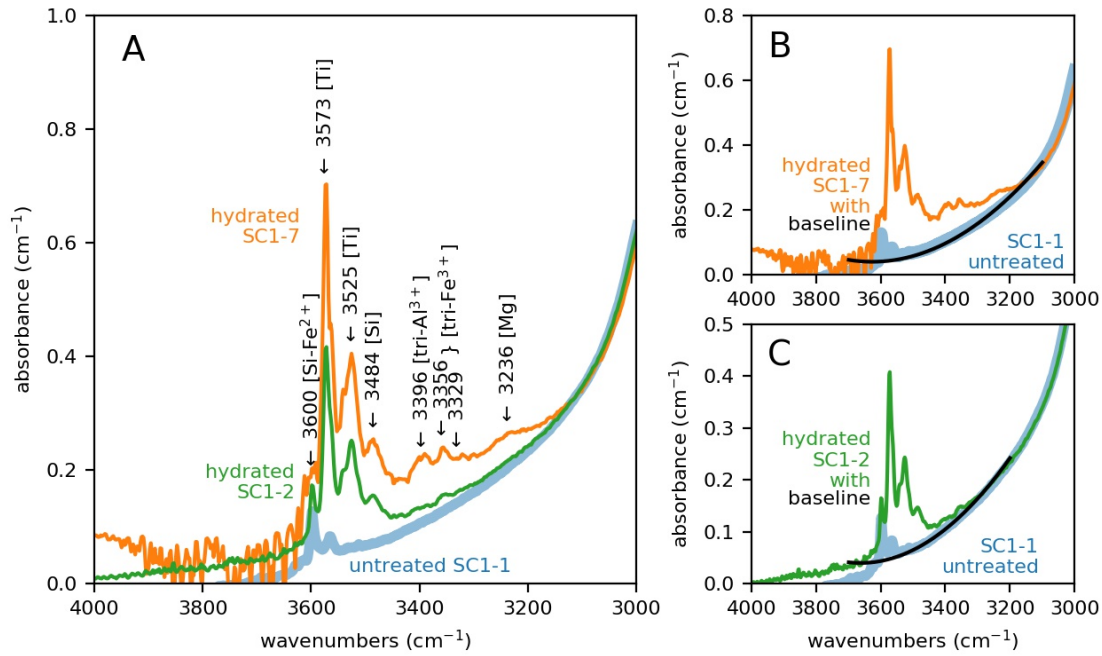


Figure 3. (A) Polarized FTIR spectra with electric vector $E \parallel a$ averaged across all traverses in three directions of San Carlos olivine SC1 pieces that were untreated (SC1-1, blue); hydrated in a piston cylinder for exactly the amount of time needed to reach “metastable equilibrium” by the proton-polaron mechanism (SC1-2, green) at 800°C; and hydrated long enough to enter into proton-vacancy-dominated diffusion without saturating the sample (SC1-7, orange) with major peaks labeled. The shapes of the quadratic baselines used to calculate the areas under each curve for spectra measured are shown for SC1-7 (B) and SC1-2 (C). Note the differences in the y-axis scale.

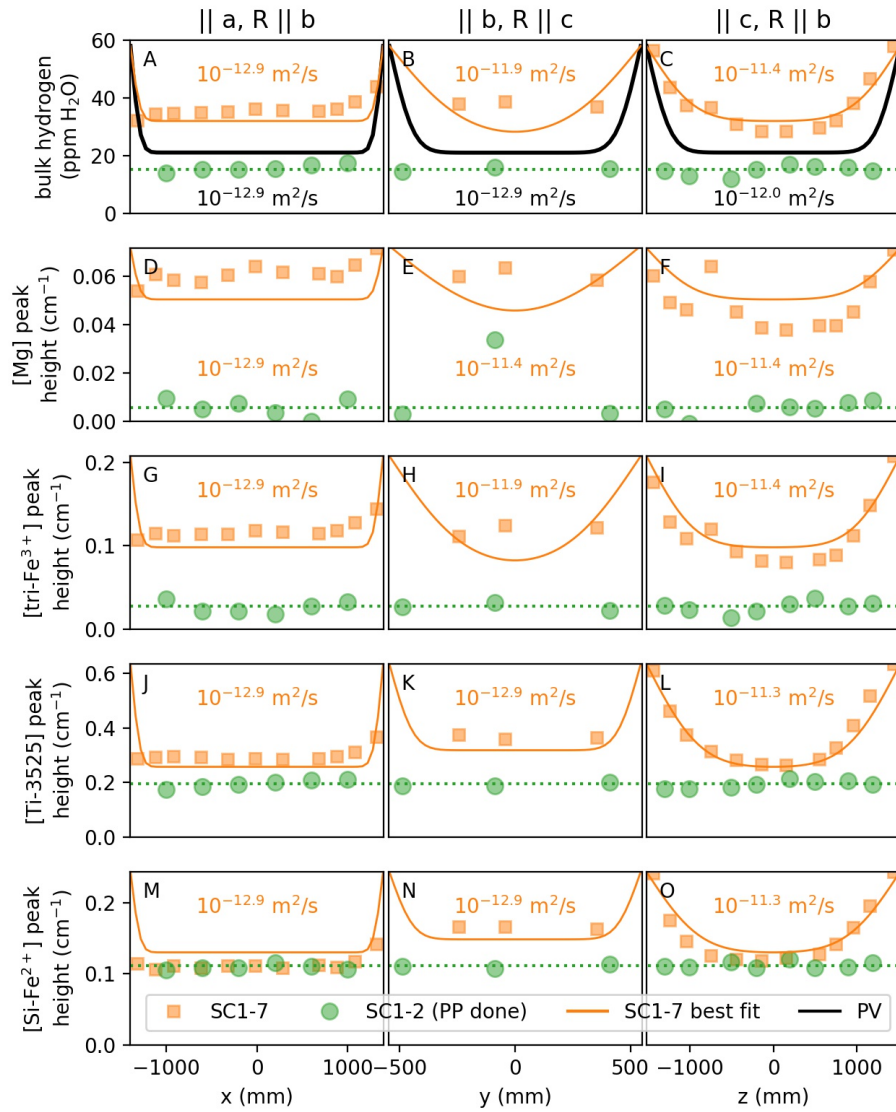


Figure 4. Concentration profiles across San Carlos olivine samples SC1-2 and SC1-7 after partial hydration in a piston cylinder as measured through the uncut block. R is the ray path of the infrared beam, and the electric vector E of the polarized beam is in all cases $\parallel a$. H^+ concentrations are estimated from polarized FTIR spectra using the areas under the baselines shown in Figure 3 and initial H^+ contents from Table 2. Black numbers and curves show the expected diffusion curves based on the diffusivities (D) for proton-vacancy (PV) mechanism diffusion at 1000°C, an initial “metastable equilibrium” concentration equal to the mean concentration or peak height in the hydrated SC1-2 (dotted green lines, where all diffusion possible by the proton-polaron (PP) mechanism has been completed) and final concentration of 58 ppm H_2O . Thin orange lines show curves for the reported diffusivities, assuming the same initial and final concentration as the PV lines. The large difference between the black and orange curves in panel A despite their having the same diffusivity is a result of path integration effects along the ray path, b , which has significantly different diffusivities for the two models. See Ferriss et al. 2015 for a more complete discussion of this “whole-block” effect.

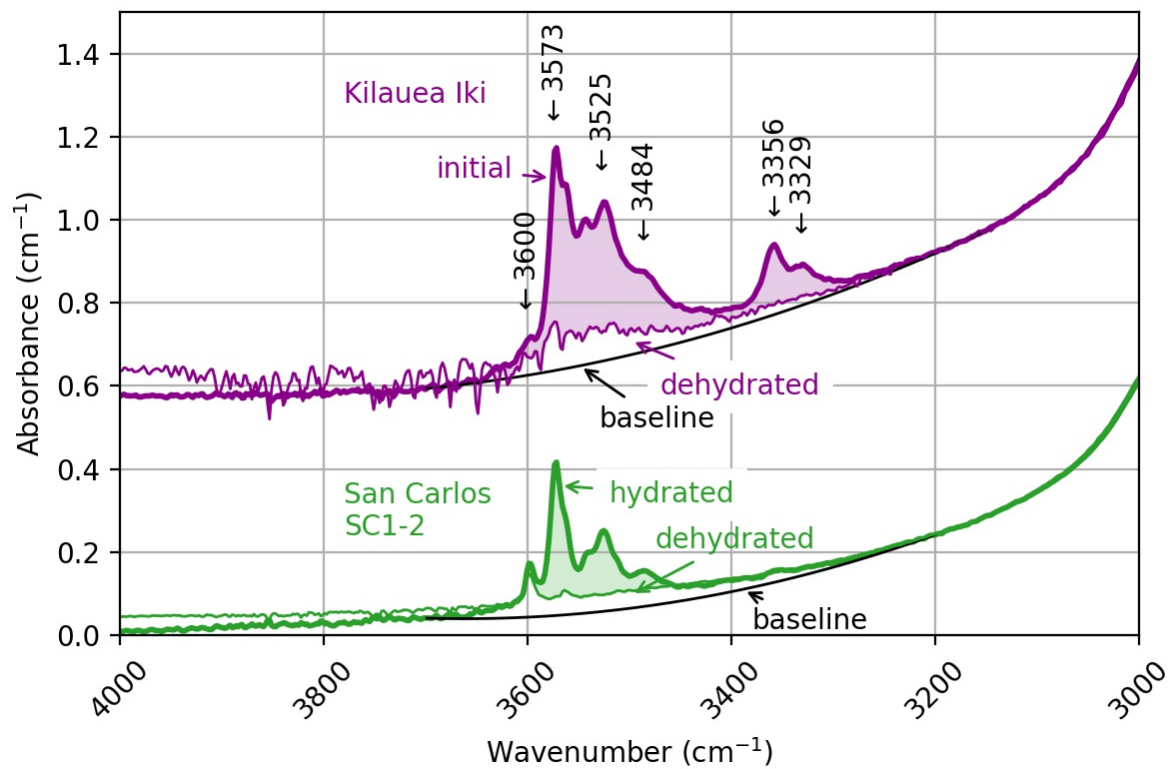


Figure 5. Averaged polarized FTIR spectra with electric vector $E \parallel a$ of Kilauea Iki olivine (offset for clarity) and partially hydrated San Carlos olivine SC1-2 before and after heating in a gas-mixing furnace.

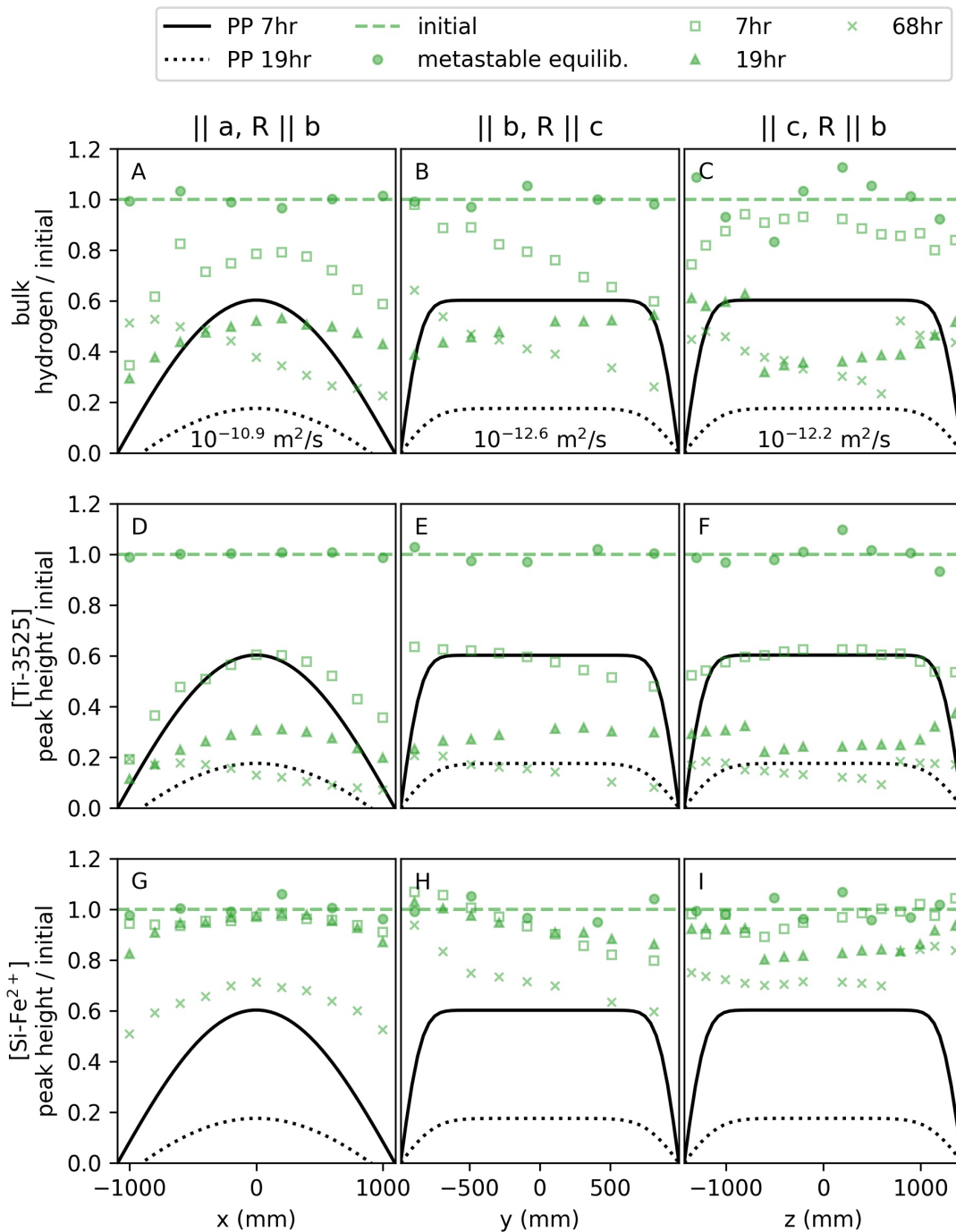


Figure 6. Path-integrated profiles of (A-C) bulk H, (D-F) the [Ti] peak at 3525 cm^{-1} , and (G-I) the [Si] peak at 3600 cm^{-1} during step-wise dehydration of an uncut block of partially hydrated San Carlos olivine SC1-2 at 1 atm, 800°C , and NNO-2.6. R is the ray path of the infrared beam. All data are normalized to a best-fit line through the hydrated profile data to account for small amounts of initial zonation. Black lines show expected hydrogen loss curves for the proton-polaron mechanism (diffusivities labeled in A-C). The PP mechanism is somewhat too fast to describe the bulk H data and much too fast to describe the [Si] peak data. The [Ti] data is very well described by the PP mechanism after 7 hours of heating, but [Ti] movement slows down by 19 hours. Baselines and best-fit diffusivities and curves are provided in the Supplemental PDF.

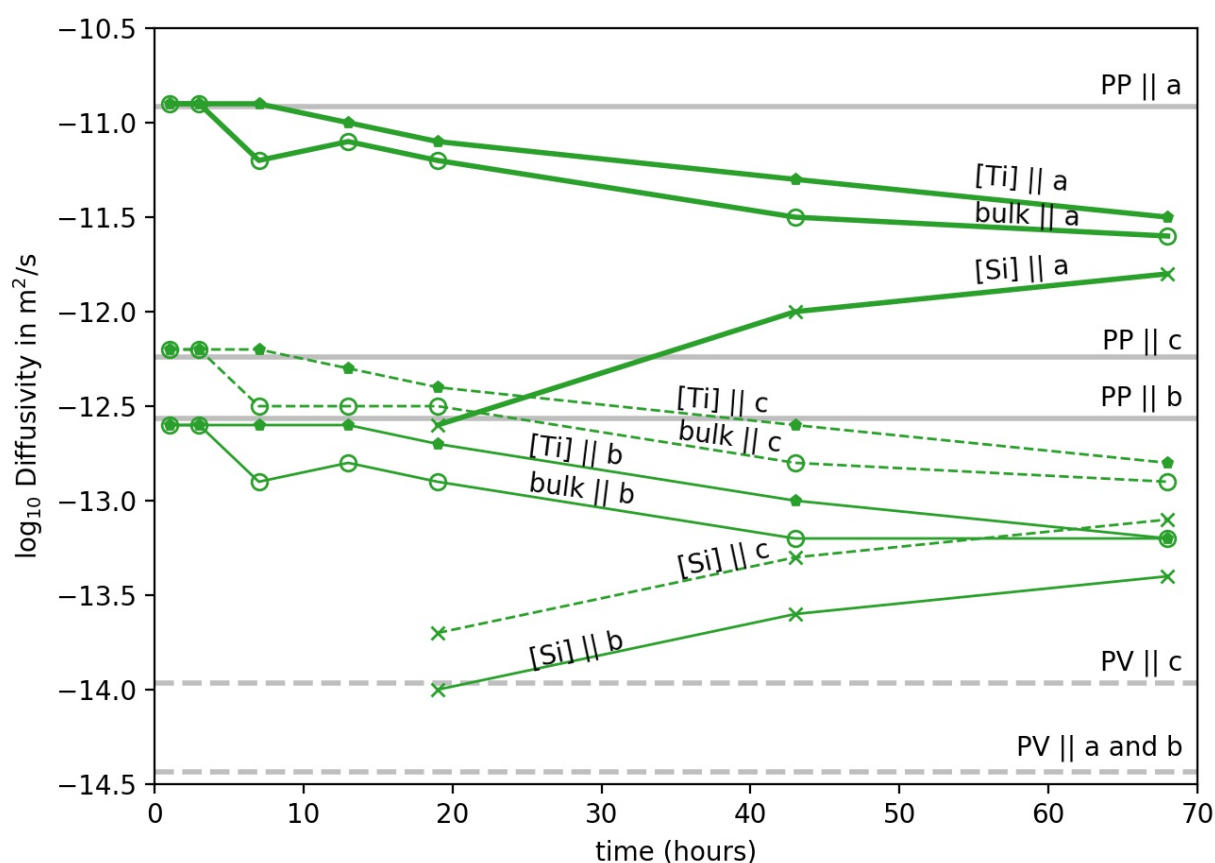


Figure 7. Estimated rates of hydrogen movement represented as diffusivities in San Carlos olivine SC1-2 with heating time at 800°C and oxygen fugacity of $10^{-16.5}$ bars (NNO-2.6) in three crystallographic directions for bulk H^+ and two peak-specific mechanisms described in the text, [Si] and [Ti], compared with expected diffusivities for the proton-polaron mechanism. Errors on all diffusivities (provided in Supplement) are omitted for clarity. The anisotropy of the observed diffusivities and PP is similar, with movement $|| a > c > b$, but the exact values are not consistent over time. At early heating stages, the bulk H^+ , which is dominated by the mechanism [Ti], is consistent with expected PP values, but over time those diffusivities decrease. In contrast, the [Si] mechanism is initially too slow to be measured confidently, but after 19 hours enough movement could be observed for fitting. These [Si] diffusivities increased at 43 and 68 hours, approaching the values for [Ti] and bulk H. The profile data used to obtain these diffusivities are shown in Figure 6 and the Supplement.

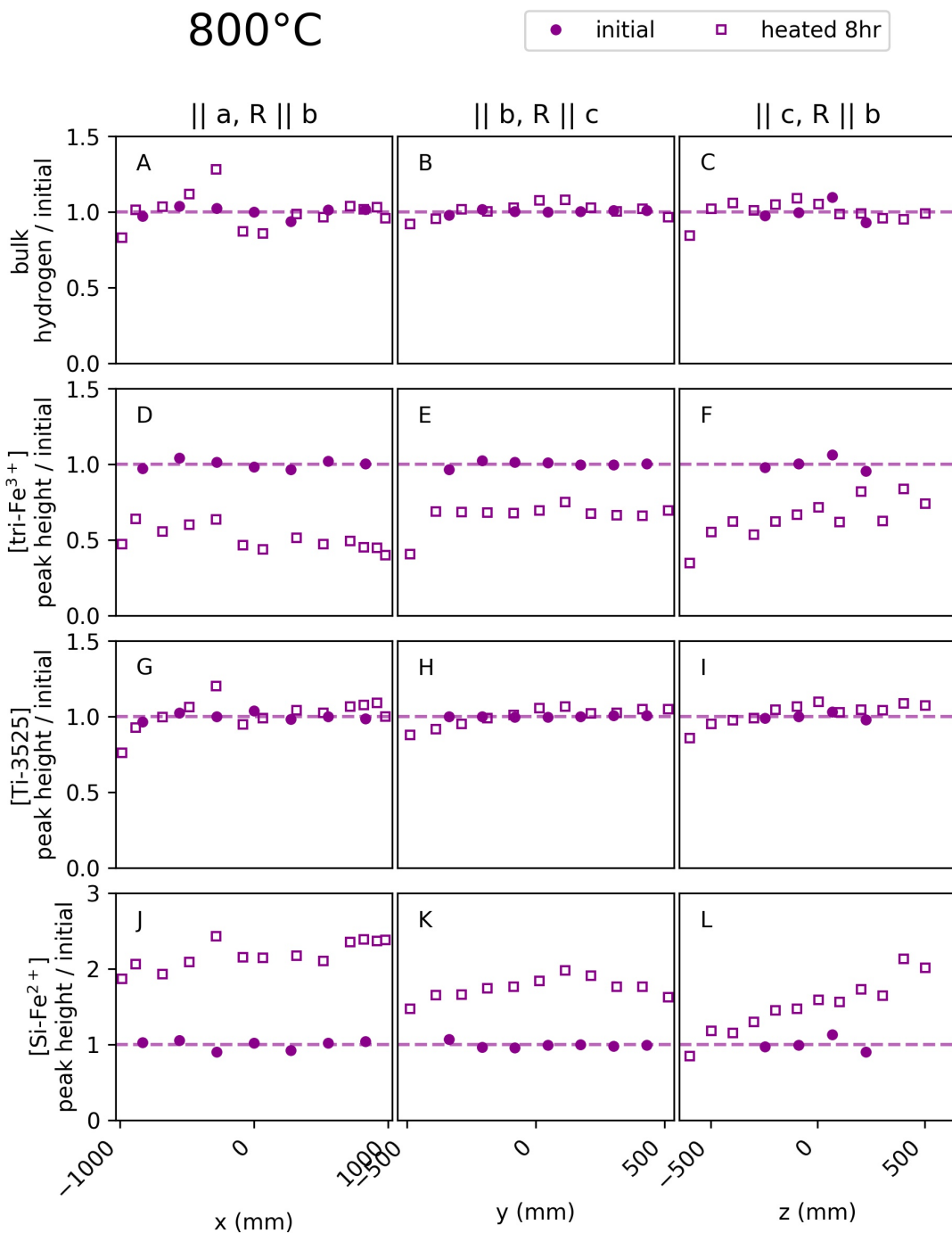


Figure 8. Path-integrated profiles of (A-C) bulk H^+ , (D-F) the $[tri-Fe^{3+}]$ peak at 3356 cm^{-1} , (G-I) the $[Ti]$ peak at 3525 cm^{-1} , and (J-L) the $[Si]$ peak at 3600 cm^{-1} in an uncut block of Kilauea Iki olivine after 8 hours of heating at 1 atm and 800°C . R is the ray path of the infrared beam. All profiles are normalized to initial profiles measured on the untreated sample.

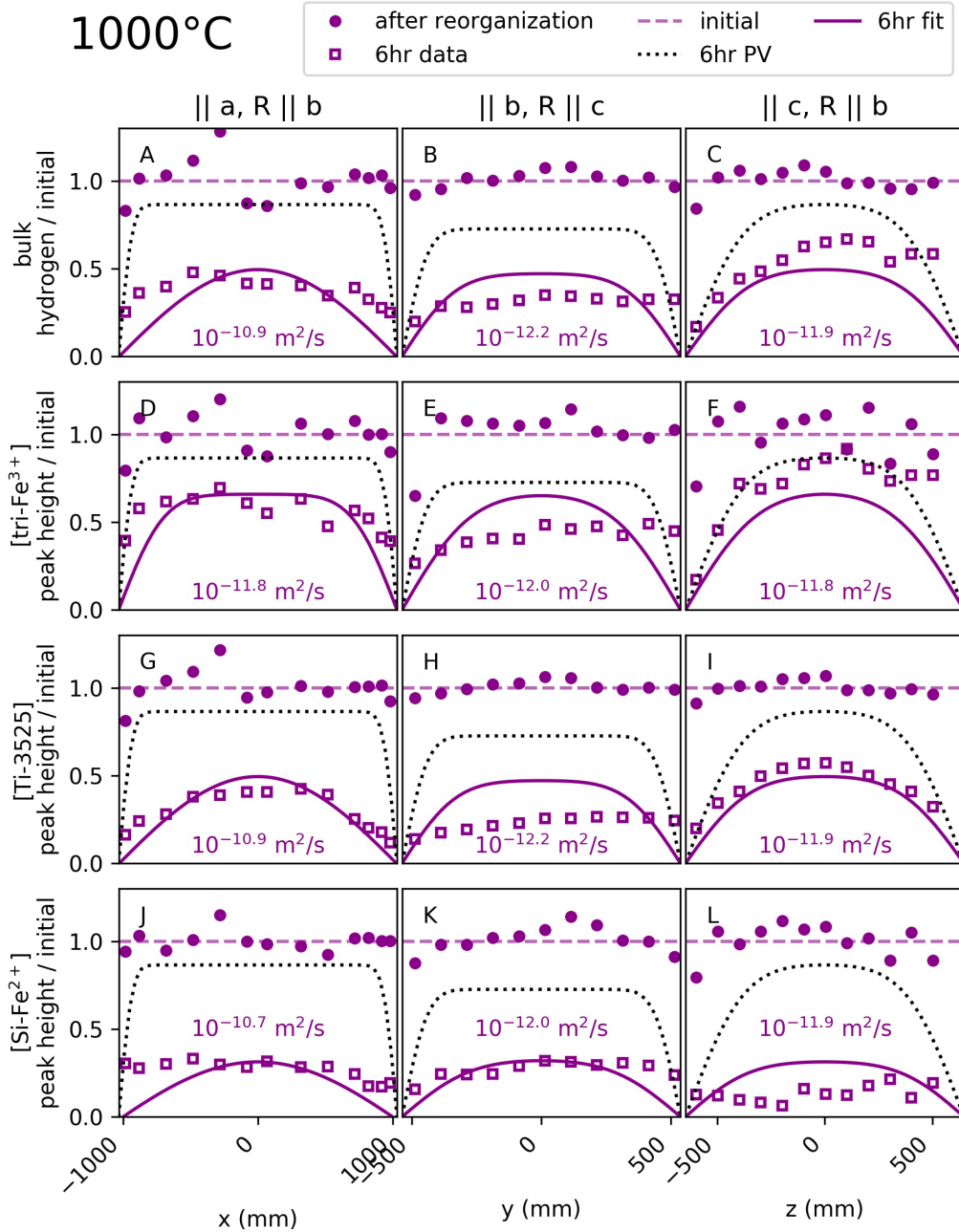


Figure 9. Path-integrated profiles of (A-C) bulk H^+ , (D-F) the $[\text{tri-Fe}^{3+}]$ peak at 3356 cm^{-1} , (G-I) the $[\text{Ti}]$ peak at 3525 cm^{-1} , and (J-L) the $[\text{Si}]$ peak at 3600 cm^{-1} in an uncut block of Kilauea Iki olivine after 6 hours of heating at 1 atm and 1000°C . R is the ray path of the infrared beam. All profiles are normalized to profile data measured after heating for 8 hours at 1 atm, 800°C , and NNO-2.6, which produced significant re-organization of the hydrogen across different sites (Figure 8). Numbers are the diffusivities that correspond to the purple lines fit to the data. The proton-vacancy mechanism (PV, dotted lines) is too slow to account for all of the observed H^+ movement. If the proton-polaron mechanism, PP, were fully active, then all H^+ would have been lost from the crystal. Baselines and best-fit diffusivities and curves are provided in the Supplement. Note the differences in x-axis scales and that this data is measured through the uncut block, and therefore measurements in the center of each profile may differ along different ray paths.

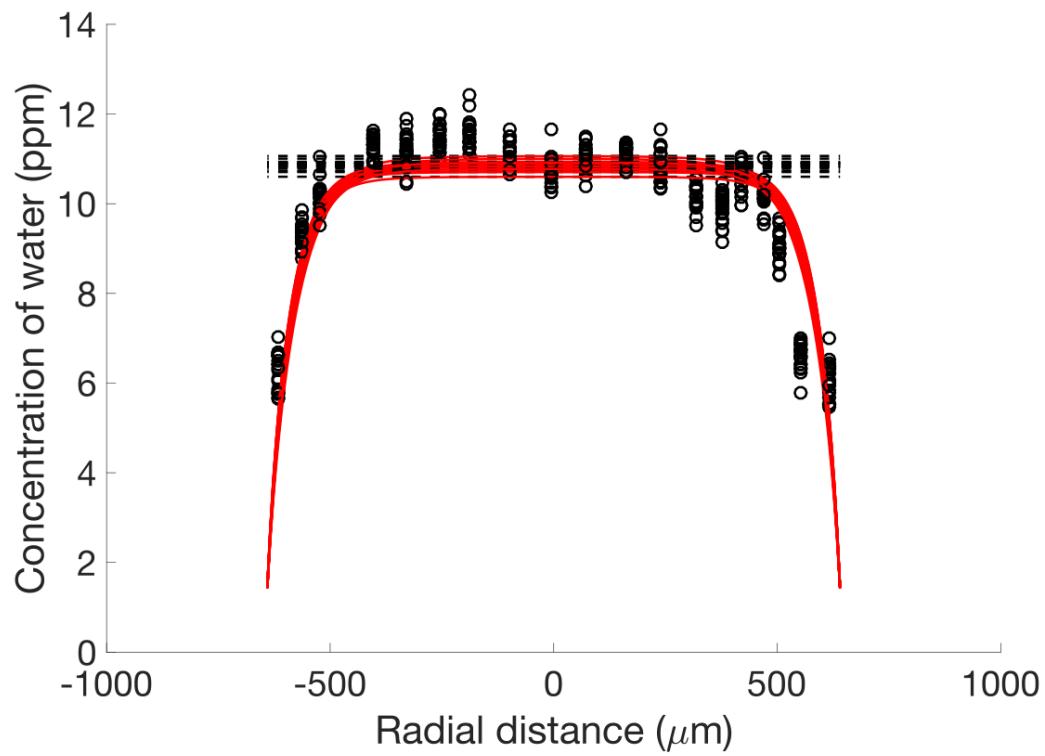


Figure 10. [Megan is making an updated figure] SIMS measurements of bulk H^+ along a in a Kilauea Iki olivine phenocryst and best-fit 1D diffusion profile assuming a diffusivity of $10^{-10} \text{ m}^2/\text{s}$ based on Monte Carlo modeling.

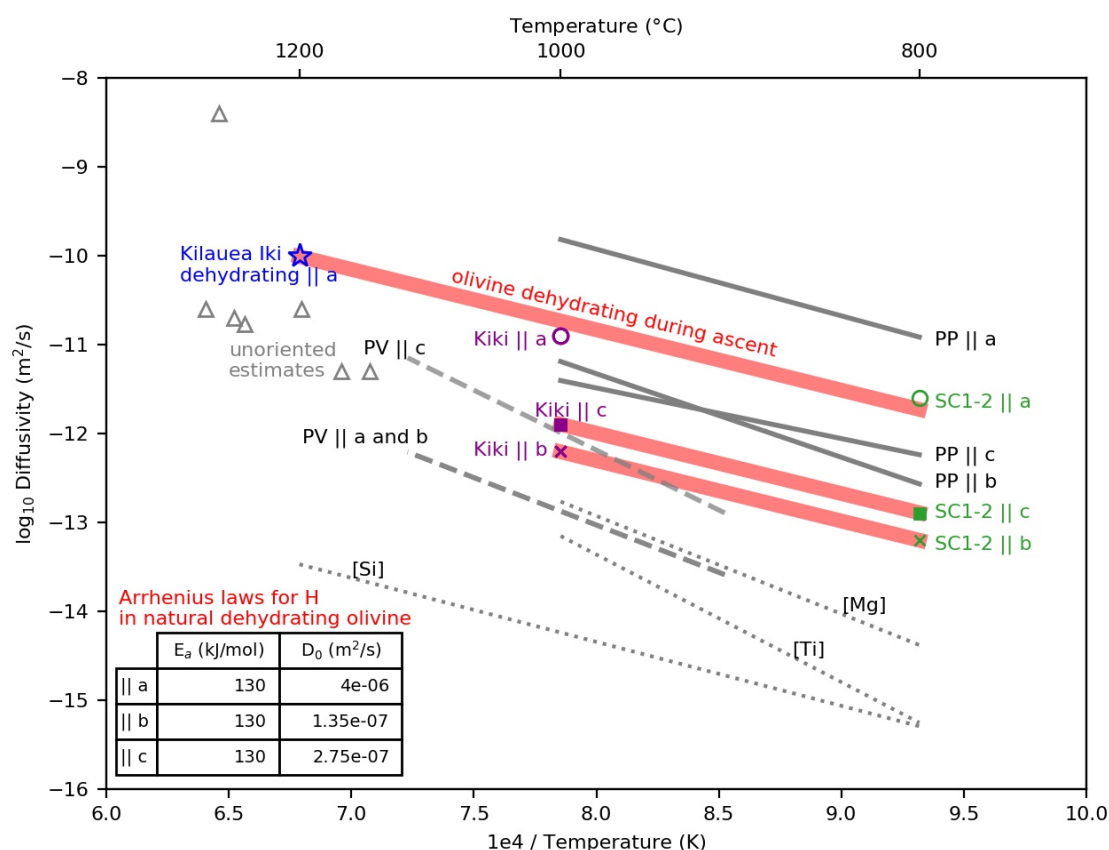


Figure 11. Arrhenius diagram for bulk H movement in olivine. Black lines show ranges for previous measurements of the proton-polaron mechanism (PP) and the proton-vacancy mechanism (PV) during hydration of San Carlos olivine as well as peak-specific measurements from the dehydration of synthetic forsterite (dotted lines, Padrón-Navarta et al. 2014). Pink line shows a fit through the final observed bulk H diffusivity measurements from this study: the experimental dehydration of San Carlos olivine at 800°C (SC1-2, green), the experimental dehydration of Kilauea Iki olivine at 1000°C (Kiki, purple), and the estimated diffusivity in Kilauea Iki || [100] during its ascent at 1200°C (blue star). Six out of seven independent estimates for bulk H diffusivity in unoriented melt-inclusion-bearing olivines (gray triangles; 1 data point from Portnyagin et al. 2008 and Mironov et al. 2015; 4 data points from Chen et al. 2011; and 1 data point from Gaetani et al. 2012) fall between and so our consistent with these fits. The exception is a higher diffusivity estimate by Hauri 2002 for an olivine from Loihi. The activation energies (E_a) and pre-exponential factors (D_0) for our fits are provided in the inset table. An interactive Arrhenius diagram that includes additional measurements and all time-series and peak-specific data is available online at <https://arrheniusdiagram.herokuapp.com>.

Bibliography

Bell, D. R., and G. R. Rossman

1992 Water in Earth's Mantle: The Role of Nominally Anhydrous Minerals. *Science* 255(5050).
WOS:A1992HH74400043: 1391–1397.

Bell, D. R., G. R. Rossman, J. Maldener, D. Endisch, and F. Rauch

2003 Hydroxide in Olivine: A Quantitative Determination of the Absolute Amount and Calibration of the IR Spectrum. *Journal of Geophysical Research-Solid Earth* 108(B2). WOS:000181985400002.
://WOS:000181985400002.

Berry, A. J., J. Hermann, H. S. C. O'Neill, and G. J. Foran

2005 Fingerprinting the Water Site in Mantle Olivine. *Geology* 33(11). WOS:000233059000008:
869–872.

Berry, A. J., A. M. Walker, J. Hermann, et al.

2007 Titanium Substitution Mechanisms in Forsterite. *Chemical Geology* 242(1–2).
WOS:000248433400010: 176–186.

Blanchard, Marc, Jannick Ingrin, Etienne Balan, István Kovács, and Anthony C. Withers

2017 Effect of Iron and Trivalent Cations on OH Defects in Olivine. *American Mineralogist* 102(2):
302–311.

Chen, Y., A. Provost, P. Schiano, and N. Cluzel

2011 The Rate of Water Loss from Olivine-Hosted Melt Inclusions. *Contributions to Mineralogy and Petrology* 162(3). WOS:000294216500011: 625–636.

Demouchy, S., and S. Mackwell

2003 Water Diffusion in Synthetic Iron-Free Forsterite. *Physics and Chemistry of Minerals* 30(8).
WOS:000185964900006: 486–494.

2006 Mechanisms of Hydrogen Incorporation and Diffusion in Iron-Bearing Olivine. *Physics and Chemistry of Minerals* 33(5). WOS:000240439000005: 347–355.

Demouchy, Sylvie, and Nathalie Bolfan-Casanova

2016 Distribution and Transport of Hydrogen in the Lithospheric Mantle: A Review. *Lithos* 240:
402–425.

Demouchy, Sylvie, Catherine Thoraval, Nathalie Bolfan-Casanova, and Geeth Manthilake

2016 Diffusivity of Hydrogen in Iron-Bearing Olivine at 3 GPa. *Physics of the Earth and Planetary Interiors* 260: 1–13.

Faul, Ulrich H., Christopher J. Cline II, Emmanuel C. David, Andrew J. Berry, and Ian Jackson

2016 Titanium-Hydroxyl Defect-Controlled Rheology of the Earth's Upper Mantle. *Earth and Planetary Science Letters* 452: 227–237.

Ferguson, David J., Helge M. Gonnermann, Philipp Ruprecht, et al.

2016 Magma Decompression Rates during Explosive Eruptions of Kīlauea Volcano, Hawaii, Recorded by Melt Embayments. *Bulletin of Volcanology* 78(10): 71.

Ferriss, E.

2015 Pynams: A Python Package for Interpreting FTIR Spectra of Nominally Anhydrous Minerals (NAMs). New York. <https://github.com/EFerriss/pynams>.

Ferriss, E., T. Plank, D. Walker, and M. Nettles

2015 The Whole-Block Approach to Measuring Hydrogen Diffusivity in Nominally Anhydrous Minerals. *American Mineralogist* 100(4). WOS:000352175700017: 837–851.

Ferriss, Elizabeth, Terry Plank, and David Walker

2016 Site-Specific Hydrogen Diffusion Rates during Clinopyroxene Dehydration. *Contributions to Mineralogy and Petrology* 171(6): 1–24.

Gaetani, G. A., J. A. O’Leary, N. Shimizu, Claire E. Bucholz, and Matthew Newville

2012 Rapid Reequilibration of H₂O and Oxygen Fugacity in Olivine-Hosted Melt Inclusions. *Geology* 40(10): 915–918.

Hauri, E.

2002 SIMS Analysis of Volatiles in Silicate Glasses, 2: Isotopes and Abundances in Hawaiian Melt Inclusions. *Chemical Geology* 183(1–4). WOS:000174332300008: 115–141.

Ingrin, J., J. Liu, C. Depecker, et al.

2013 Low-Temperature Evolution of OH Bands in Synthetic Forsterite, Implication for the Nature of H Defects at High Pressure. *Physics and Chemistry of Minerals* 40(6). WOS:000319771000005: 499–510.

Jollands, Michael C., José Alberto Padrón-Navarta, Jörg Hermann, and Hugh St.C. O’Neill

2016 Hydrogen Diffusion in Ti-Doped Forsterite and the Preservation of Metastable Point Defects. *American Mineralogist* 101(7): 1560–1570.

Keppler, Hans, and Joseph R. Smyth

2006 Water in Nominally Anhydrous Minerals, vol.62. *Reviews in Mineralogy and Geochemistry*. Mineralogical Society of America.

Kohlstedt, D. L., and S. J. Mackwell

1998 Diffusion of Hydrogen and Intrinsic Point Defects in Olivine. *Zeitschrift Fur Physikalische Chemie-International Journal of Research in Physical Chemistry & Chemical Physics* 207. WOS:000076569300010: 147–162.

Kurosawa, M., H. Yurimoto, and S. Sueno

1997 Patterns in the Hydrogen and Trace Element Compositions of Mantle Olivines. *Physics and Chemistry of Glasses* 24: 385–395.

Le Voyer, Marion, Paul D. Asimow, Jed L. Mosenfelder, et al.

2014 Zonation of H₂O and F Concentrations around Melt Inclusions in Olivines. *Journal of Petrology* 55(4): 685–707.

Libowitzky, E., and G. R. Rossman

1996 Principles of Quantitative Absorbance Measurements in Anisotropic Crystals. *Physics and Chemistry of Minerals* 23(6). WOS:A1996VD85000001: 319–327.

Lloyd, Alexander S., T. Plank, Philipp Ruprecht, E. H. Hauri, and William Rose

2013 Volatile Loss from Melt Inclusions in Pyroclasts of Differing Sizes. *Contributions to Mineralogy and Petrology* 165: 129–153.

Mackwell, S. J., and D. L. Kohlstedt

1990 Diffusion of Hydrogen in Olivine - Implications for Water in the Mantle. *Journal of Geophysical Research-Solid Earth and Planets* 95(B4). WOS:A1990CZ37500052: 5079–5088.

Mironov, Nikita, Maxim Portnyagin, Roman Botcharnikov, et al.

2015 Quantification of the CO₂ Budget and H₂O–CO₂ Systematics in Subduction-Zone Magmas through the Experimental Hydration of Melt Inclusions in Olivine at High H₂O Pressure. *Earth and Planetary Science Letters* 425: 1–11.

Mosenfelder, J. L., N. I. Deligne, P. D. Asimow, and G. R. Rossman

2006 Hydrogen Incorporation in Olivine from 2-12 GPa. *American Mineralogist* 91(2–3). WOS:000235472000007: 285–294.

Padrón-Navarta, Jose Alberto, Joerg Hermann, and Hugh St. C. O'Neill

2014 Site-Specific Hydrogen Diffusion Rates in Forsterite. *Earth and Planetary Science Letters* 392: 100–112.

Peslier, A. H., and J. F. Luhr

2006 Hydrogen Loss from Olivines in Mantle Xenoliths from Simcoe (USA) and Mexico: Mafic Alkalic Magma Ascent Rates and Water Budget of the Sub-Continental Lithosphere. *Earth and Planetary Science Letters* 242(3–4). WOS:000235855100006: 302–319.

Portnyagin, M., Renat Almeev, S. Matveev, and Francois Holtz

2008 Experimental Evidence for Rapid Water Exchange between Melt Inclusions in Olivine and Host Magma. *Earth and Planetary Science Letters* 272: 541–552.

Rosen, Julia

2016 Crystal Clocks. *Science* 354(6314): 822–825.

Ruprecht, Philipp, and Terry Plank

2013 Feeding Andesitic Eruptions with a High-Speed Connection from the Mantle. *Nature* 500(7460): 68–72.

Shuai, Kang, and Xiaozhi Yang

2017 Quantitative Analysis of H-Species in Anisotropic Minerals by Polarized Infrared Spectroscopy along Three Orthogonal Directions. *Contributions to Mineralogy and Petrology* 172(2–3): 14.

Thoraval, Catherine, and Sylvie Demouchy

2014 Numerical Models of Ionic Diffusion in One and Three Dimensions: Application to Dehydration of Mantle Olivine. *Physics and Chemistry of Minerals* 41(9). WOS:000341924800005: 709–723.

Tollan, P. M. E., H. St C. O'Neill, J. Hermann, A. Benedictus, and R. J. Arculus

2015 Frozen Melt-Rock Reaction in a Peridotite Xenolith from Sub-Arc Mantle Recorded by Diffusion of Trace Elements and Water in Olivine. *Earth and Planetary Science Letters* 422. WOS:000355350700018: 169–181.

Tollan, Peter M. E., Rachel Smith, Hugh St C. O'Neill, and Jörg Hermann

2017 The Responses of the Four Main Substitution Mechanisms of H in Olivine to H₂O Activity at 1050 °C and 3 GPa. *Progress in Earth and Planetary Science* 4(1): 14.

Withers, A. C.

2013 The Pitzer and Sterner Equation of State for Water.

<http://www.geo.umn.edu/people/researchers/withe012/fugacity.htm>, accessed August 6, 2013.

Withers, Anthony C, Hélène Bureau, Caroline Raepsaet, and Marc M Hirschmann

2012 Calibration of Infrared Spectroscopy by Elastic Recoil Detection Analysis of H in Synthetic Olivine. *Chemical Geology* 334: 92–98.

Zhao, Y. H., S. B. Ginsberg, and D. L. Kohstedt

2004 Solubility of Hydrogen in Olivine: Dependence on Temperature and Iron Content. *Contributions to Mineralogy and Petrology* 147(2). WOS:000221169500003: 155–161.